Cell Reports

Article

Structural basis for GTPase activity and conformational changes of the bacterial dynamin-like protein *Syn*DLP

Graphical abstract

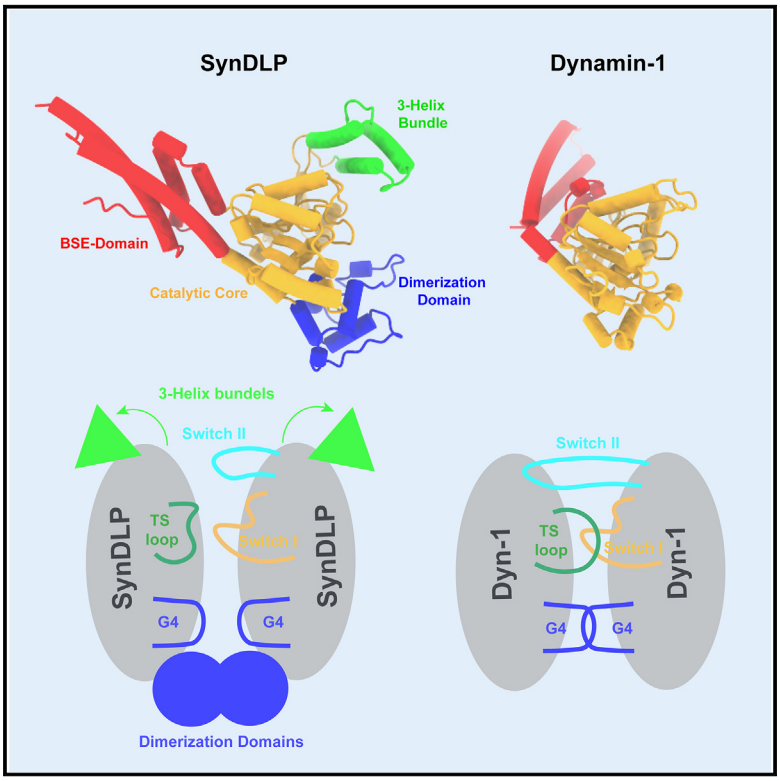

Authors

Benedikt Junglas, Lucas Gewehr, Lara Mernberger, ..., Nadja Hellmann, Dirk Schneider, Carsten Sachse

Correspondence

dirk.schneider@uni-mainz.de (D.S.), c.sachse@fz-juelich.de (C.S.)

In brief

*Syn*DLP is a cyanobacterial dynamin-like protein. Junglas et al. show the structures of *Syn*DLP incubated with nucleotides and the structure of a GMPPNP-bound minimal GD construct that dimerizes via an unique extended dimerization domain not present in canonical G-domains.

Highlights

- Cryo-EM structures of *Syn*DLP with GDP and GTP
- Cryo-EM structure of GMPPNP-bound *Syn*DLP minimal GD construct
- *Syn*DLP GDs dimerize via an unique extended dimerization domain
- *Syn*DLP remodels membranes

Junglas et al., 2024, Cell Reports *43*, 114657
September 24, 2024
https://doi.org/10.1016/j.celrep.2024.114657

CellPress

Cell Reports

CellPress
OPEN ACCESS

Article

Structural basis for GTPase activity and conformational changes of the bacterial dynamin-like protein *Syn*DLP

Benedikt Junglas,[1,5] Lucas Gewehr,[2,5] Lara Mernberger,[2] Philipp Schönnenbeck,[1] Ruven Jilly,[2] Nadja Hellmann,[2] Dirk Schneider,[2,3,*] and Carsten Sachse[1,4,6,*]

[1]Ernst Ruska-Center for Microscopy and Spectroscopy with Electrons (ER-C-3): Structural Biology, Forschungszentrum Jülich, 52425 Jülich, Germany

[2]Department of Chemistry, Biochemistry, Johannes Gutenberg University Mainz, 55128 Mainz, Germany

[3]Institute of Molecular Physiology, Johannes Gutenberg University Mainz, 55128 Mainz, Germany

[4]Department of Biology, Heinrich Heine University, 40225 Düsseldorf, Germany

[5]These authors contributed equally

[6]Lead contact

*Correspondence: dirk.schneider@uni-mainz.de (D.S.), c.sachse@fz-juelich.de (C.S.)

https://doi.org/10.1016/j.celrep.2024.114657

SUMMARY

*Syn*DLP, a dynamin-like protein (DLP) encoded in the cyanobacterium *Synechocystis* sp. PCC 6803, has recently been identified to be structurally highly similar to eukaryotic dynamins. To elucidate structural changes during guanosine triphosphate (GTP) hydrolysis, we solved the cryoelectron microscopy (cryo-EM) structures of oligomeric full-length *Syn*DLP after addition of guanosine diphosphate (GDP) at 4.1 Å and GTP at 3.6-Å resolution as well as a GMPPNP-bound dimer structure of a minimal G-domain construct of *Syn*DLP at 3.8-Å resolution. In comparison with what has been seen in the previously resolved apo structure, we found that the G-domain is tilted upward relative to the stalk upon GTP hydrolysis and that the G-domain dimerizes via an additional extended dimerization domain not present in canonical G-domains. When incubated with lipid vesicles, we observed formation of irregular tubular *Syn*DLP assemblies that interact with negatively charged lipids. Here, we provide the structural framework of a series of different functional *Syn*DLP assembly states during GTP turnover.

INTRODUCTION

Dynamins and dynamin-like proteins (DLPs) are involved in various membrane remodeling processes, including fission and fusion of vesicles or organelle membranes.[1–8] DLPs have also been identified in bacteria.[9] Although the physiological function of bacterial DLPs (BDLPs) is unknown in most cases, and BDLPs appear to be involved in membrane fission or fusion like their eukaryotic counterparts.[10–12] DLPs are large mechano-chemical GTPases that differ from small Ras-like GTPases by their oligomerization-dependent GTPase activation and their membrane interaction mode.[13] DLPs are typically not highly conserved on the sequence level, and their identity is mostly defined by the presence of certain common structural elements. DLPs consist of a globular GTPase domain (GD), followed by the bundle signaling element (BSE), an α-helical stalk or trunk domain, and a variable membrane interaction domain (MID). These domains are connected by flexible hinges that enable major conformational changes,[14,15] resulting in a structural flexibility critical for the DLP membrane remodeling activity. On the sequence level, the GD is the only conserved element of DLPs, as it contains the typical guanosine triphosphate (GTP)-binding motifs, including the P loop, G2 motif/switch I, G3 motif/switch II, and G4 motif. As for most GTPases, the core GD consists of ∼160 amino acids (aa) forming a mixed six-stranded β sheet surrounded by five α helices. In the case of DLPs, this core GD is extended to ∼300 aa and typically has a low GTP binding affinity.[13,15]

A typical DLP GTPase cycle consists of GTP binding, GTP hydrolysis, and guanosine diphosphate (GDP) release. The energy released by GTP hydrolysis leads to a conformational change that triggers a rearrangement of the neighboring domains. In contrast to Ras-like GTPases, which cannot oligomerize and require a GTPase-activating protein (GAP) for efficient GTP hydrolysis, DLPs function as their own GAPs, and DLP homo-oligomerization stimulates the GTPase activity.[14,16] Consequently, the GTPase activity of DLPs typically increases when smaller DLP assemblies oligomerize. On the molecular level, the cooperativity is commonly realized by intermolecular GD contacts leading to a head-to-head dimerization of adjacent GDs from DLPs oligomerized in a helical array.[17–19] Prototypical Dynamin-1, a DLP mediating membrane fission, forms dimers or tetramers in solution via interactions in the stalk domain while it further oligomerizes on a membrane surface into tube-forming, helical

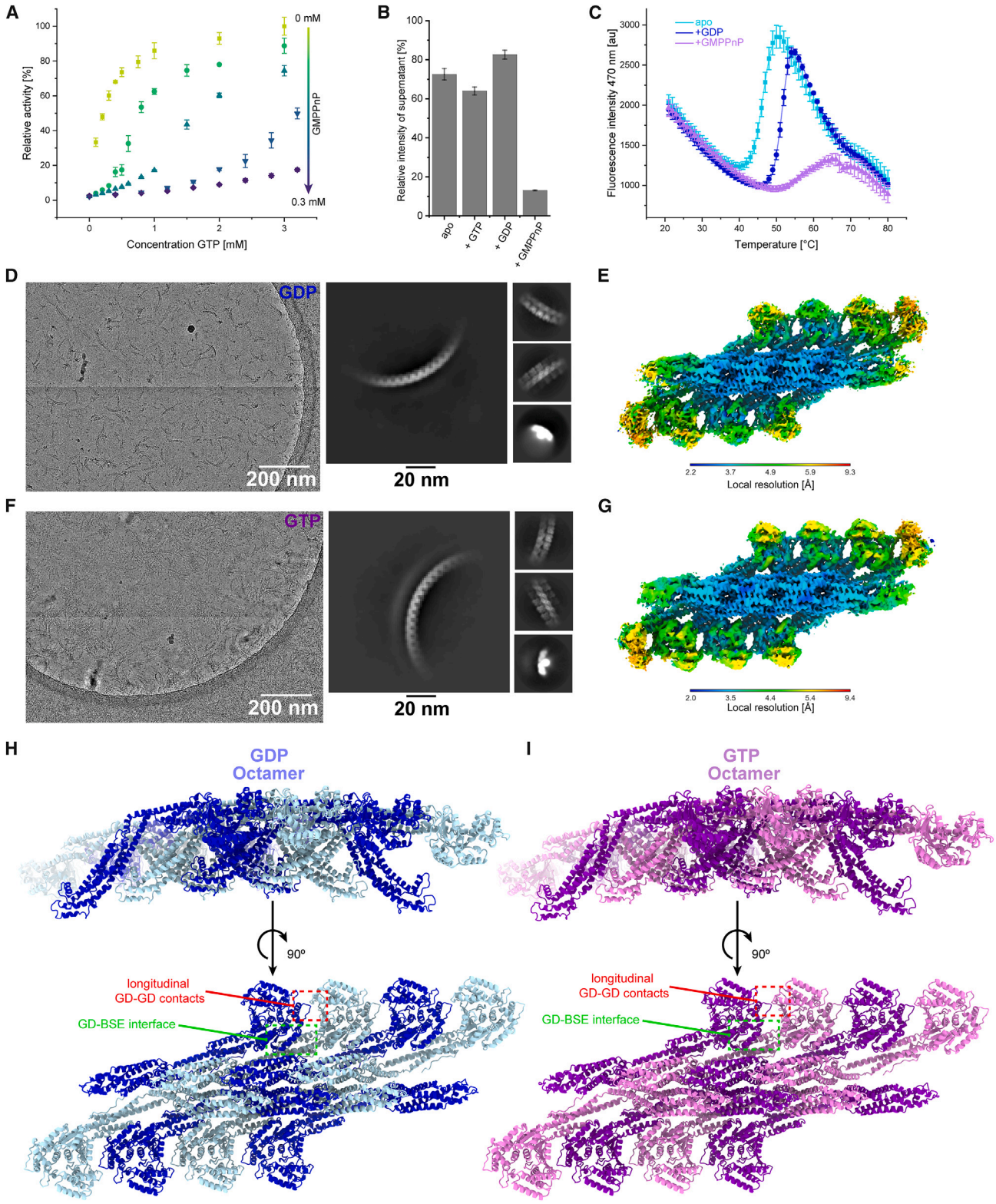

Figure 1. The structure of *Syn*DLP oligomers after addition of nucleotides

(A) The GTPase activity of *Syn*DLP determined in the presence of increasing concentrations of GMPPNP (0, 0.05, 0.1, 0.2, and 0.3 mM, yellow-to-blue gradient). Error bars represent SD; $n \geq 2$.

(legend continued on next page)

filaments. Subsequently, dimerization of GDs from adjacent rungs within the helical oligomer is established in a head-to-head fashion, followed by GTP hydrolysis. The GTP hydrolysis energy leads to a conformational change mediated by domain movements enabled by the flexible hinges. This domain rearrangement results in a power stroke by a movement of the helical turns against each other, finally constricting the membrane tube into a hemi-fission state. Thereafter, the GD-GD dimers are destabilized and dissociate, followed by GDP release. A recovery stroke is initiated by the binding of a new GTP molecule at the active site. Next, a GD dimerizes with the next GD on the adjacent rung of the filament, and the entire cycle repeats. The diameter of the membrane tube is reduced by approximately 1 nm during each cycle, and, thus, several cycle repetitions are necessary for full membrane fission.[17,20,21]

For most DLPs, a basal GTPase activity of ~1 min^{-1} was determined in solution. Upon binding to membranes, the GTPase activity increases more than 100-fold due to DLP oligomerization on membrane surfaces involving the formation of activating GD-GD contacts.[15,17,22–24] For many DLPs, oligomerization on the membrane and the formation of a helical array has been visualized *in vitro* by electron microscopy as tubulated vesicles.[11,25–29] Typically, longitudinal oligomerization of DLPs is mainly mediated by defined intermolecular contacts in the α-helical stalk domain.[30–32] The analyses of so-called minimal GD (MGD) constructs has been established as a tool to study adjustments in the GD structure and interactions induced by nucleotide binding.[17,33–36] MGDs are truncated DLP variants with an omitted stalk domain/MID and, thus, consist of solely the GD and the BSE domain, making them well-suited constructs for monitoring structural changes in the GD/BSE domain during a GTP hydrolysis cycle.[17,37]

Recently, a BDLP from the cyanobacterium *Synechocystis* sp. PCC 6803 has been described (*Syn*DLP) whose basic tertiary structure organization was found to be highly similar to eukaryotic Dynamin-3.[38] *Syn*DLP forms, already in solution, short filamentous oligomers containing approximately 40–50 molecules. The cryo-EM structure of these oligomers revealed intra-oligomeric stalk interfaces typical for many DLPs. The BSE domain of *Syn*DLP has distinct molecular features, such as an intramolecular disulfide bond or an expanded intermolecular interface with a neighboring GD. Further, the *Syn*DLP oligomer structure reveals longitudinal GD-GD contacts, as observed in filaments of the eukaryotic DLP Drp1.[31] *Syn*DLP has an unusually high basal GTPase activity of ~45 min^{-1} already in solution, most likely due to its intrinsic propensity to form higher-ordered oligomeric structures already in the absence of membranes and the resulting intermolecular GD-BSE interactions.[38] Although *Syn*DLP has been shown to bind to negatively charged membrane surfaces, the GTPase activity of *Syn*DLP is not stimulated in the presence of lipid membranes.[38] Upon membrane binding, *Syn*DLP remodels negatively charged membranes, leading to vesicle fusion by a thus far unknown mechanism. Therefore, *Syn*DLP has been classified as a fusogenic BDLP. As *Bs*DynA, a fusogenic BDLP from *Bacillus subtilis*, has been shown to be involved in membrane repair and phage defense,[10,39–41] *Syn*DLP may also be involved in stabilization and/or the repair of membranes.[38]

In the current study, we determined the cryoelectron microscopy (cryo-EM) structures of filamentous *Syn*DLP oligomers after addition of GDP at 4.1-Å and GTP at 3.6-Å resolution as well as the GMPPNP-bound dimer structure of an MGD construct of *Syn*DLP at 3.8-Å resolution. We found that the GD is tilted upward relative to the stalk upon GTP binding/hydrolysis. While the catalytic core of the *Syn*DLP GD is similar to the canonical GD of dynamins, GD dimerization is rather mediated by an extended dimerization domain than by the canonical *trans*-stabilizing loop residues known from other DLPs. Moreover, in the presence of lipid membranes, we observed the formation of irregular *Syn*DLP tubular assemblies.

RESULTS

The structure of SynDLP oligomers changes after addition of nucleotides

Previously, we determined the cryo-EM structure of *Syn*DLP oligomers in the absence of nucleotides.[38] In the determined short filamentous oligomers, we observed atypical longitudinal GD-GD contacts, which have been hypothesized to be responsible for the high basal activity, at least in part. The dependence of the wild-type *Syn*DLP steady-state GTPase activity on the GTP concentration can be described by a hyperbolic Michaelis-Menten curve,[38] which, however, does not allow unambiguous determination of dimerization and Michaelis-Menten constants, even when considering the dependence of the activity on the protein concentration. To obtain further insights into the activation mechanism, we next investigated the effect of the non-hydrolyzable GTP analog GMPPNP on the *Syn*DLP GTPase activity (Figure 1A). The presence of 0.05 or 0.1 mM GMPPNP led to sigmoidal curves with a steep increase around the inflection points (around 0.6 and 1.4 mM GTP). However, the observed changes in the GTPase activity in the presence of GMPPNP cannot be well fitted with a model that assumes competitive binding and a (simple) monomer-dimer equilibrium (Figure S1A). Further increasing the GMPPNP concentration resulted in curves with increasing GTPase activity

(B) Sedimentation of *Syn*DLP in the presence of different nucleotides. A representative SDS gel is shown in Figure S1A. Error bars represent SD; $n = 3$. Data obtained with the apo protein or after addition of GDP or GTP are taken from Gewehr et al.[38]
(C) Thermal shift assay of *Syn*DLP with and without GDP and GMPPNP. Cyan, *Syn*DLP apo; blue, *Syn*DLP+GDP; violet, *Syn*DLP+GMPPNP. Error bars represent SD; $n = 3$.
(D and F) Cryo-EM micrograph and 2D class averages of *Syn*DLP+GDP (D) and SynDLP+GTP (F). Left: a 2D class average of uncropped *Syn*DLP filamentous oligomers. Right: different close-up views of particles with a box size of 391 Å.
(E and G) Cryo-EM density map of *Syn*DLP filamentous oligomers with GDP (E) and GTP (G), colored by local resolution.
(H and I) Atomic model of the *Syn*DLP oligomer in the presence of GDP/GTP in ribbon representation. The intermolecular GD-GD and GD-BSE interfaces are marked in red and green, respectively.

Table 1. Cryo-EM sample details

Sample details	SynDLP GTP	SynDLP GDP	SynDLP apo	SynDLP MGD GMPPNP	SynDLP apo DOPG	SynDLP GDP DOPG	SynDLP GMPPNP DOPG	DOPG
Protein conc.	5.0 mg/mL	5.0 mg/mL	3.0 mg/mL	3.5 mg/mL	0.5 mg/mL	0.5 mg/mL	0.5 mg/mL	–
Lipid conc.	–	–	–	–	5.0 mg/mL	5.0 mg/mL	5.0 mg/mL	5.0 mg/mL
NTP conc.	1 mM	1 mM	–	1 mM	–	2 mM	2 mM	–
Magnification	49 kx	49 kx	49 kx	100 kx	39 kx	39 kx	39 kx	39 kx
Physical pixel size	1.737 Å[a]	1.737 Å[a]	1.737 Å[a]	0.816 Å	2.198 Å	2.198 Å	2.198 Å	2.198 Å
Frames	70	70	30	40	30	30	30	30
Total dose	44.5 e–/Å^2	44.5 e–/Å^2	26.5 e–/Å^2	80.0 e–/Å^2	48.7 e–/Å^2	49.5 e–/Å^2	49.5 e–/Å^2	49.5 e–/Å^2
Defocus range	1.0 to 3.5 μm	1.0 to 3.5 μm	2.0 to 4.0 μm	1.25 to 2.50 μm	2.0 to 4.0 μm	2.0 to 4.0 μm	2.0 to 4.0 μm	2.0 to 4.0 μm
Videos	4,560	6,149	8,322	5,087	681	210	327	786

[a]Processed in super-resolution with 0.8685 Å/pixel.

without any sigmoidal shape in the GTP concentration range investigated. Thus, these data were not analyzed further. Based on these observations, the inhibitory effect of GMPPNP cannot be explained by assuming a simple monomer-dimer equilibrium, while it indicates a more complex mechanism of oligomerization and/or activation.

As apo *Syn*DLP forms oligomeric assemblies in solution, we next tested, through sedimentation analyses, whether nucleotide binding and/or hydrolysis further affect oligomerization of *Syn*DLP (Figures 1B and S1B). In the apo form as well as with GDP or GTP, respectively, *Syn*DLP has been found to be mostly soluble in the supernatant.[38] We also tested sedimentation in the presence of the non-hydrolyzable GTP analog GMPPNP. Here, we found *Syn*DLP mostly in the pellet fraction, indicating that the *Syn*DLP structure or assembly state changes when the non-hydrolyzable GTP analog is bound, and *Syn*DLP appears to form larger assemblies in the presence of GMPPNP. Thus, GMPPNP does not just compete with GTP, as already concluded based on the enzymatic data, but also alters the assembly structure. Therefore, we next analyzed the structure of *Syn*DLP in the presence of non-hydrolyzable GTP analogs by negative staining EM and cryo-EM and found that *Syn*DLP forms ill-defined assemblies upon addition of GMPPNP or GMPPCP instead of well-defined, short filamentous oligomers (Figure S1C). When the thermal stability of the *Syn*DLP tertiary and/or quaternary structure was analyzed by an 8-anilinonaphthalene-1-sulfonic acid (ANS) fluorescence thermal shift assay in the presence of GDP or GMPPNP, the melting temperature increased from 46.7°C ± 0.1°C (apo) to 51.8°C ± 0.1°C (GDP) or 57.0°C ± 0.8°C (GMPPNP), respectively (Figure 1C), again indicating that nucleotide binding affects the structure of *Syn*DLP. Note that the GTP-bound state of *Syn*DLP could not be measured by an ANS fluorescence thermal shift assay due to the long measurement time and the high GTPase activity of the protein. Together, the combined observations suggest the formation of structurally distinct and more stable *Syn*DLP assemblies when GDP or GMPPNP are bound.

To elucidate the described changes at the molecular level, we next set out to solve the structures of *Syn*DLP with GDP or GTP, using a segmented single-particle cryo-EM workflow. As already observed in the apo state,[38] *Syn*DLP forms curved half-moon-shaped filamentous oligomers also in the presence of GDP and GTP with a length of about 100 nm and a curvature radius of 50–55 nm (Figures 1D and 1F; Table 1). Furthermore, the cryo-EM reconstructions of the *Syn*DLP oligomers revealed very similar overall molecular dimensions and appearances as the apo state structure (Figures 1E and 1G; Table 2). The cryo-EM structures were resolved at 3.6-Å and 4.1-Å resolution according to the FSC (0.143) cutoff for the structures solved after addition of GDP and GTP, respectively (Figures S1C and S1D; Table 2). For the structure with GTP, the local resolution varied from 3.5–3.7 Å in the stalk domain and from 4.0–5.4 Å in the GD, whereas for the GDP-bound structure the local resolution varied from 3.7–4.0 Å in the stalk domain and from 4.4–5.9 Å in the GD. Notably, the GD had the overall poorest resolution, and, therefore, the density did not allow placement of the bound nucleotides. In both cases, the segmented density enclosed 2 × 4 *Syn*DLP monomers in the typical antiparallel *Syn*DLP arrangement (Figures 1H and 1I). The apo state and the states of *Syn*DLP incubated with nucleotides share the basic structural elements and overall domain architecture (Figures S1E and 1F). Moreover, as observed previously for the apo state, after addition of nucleotides, the BSE bundle forms an extended intermolecular interface with the GD, and the neighboring GDs interact longitudinally via a short loop region (aa 389–394). Detailed inspection of the determined cryo-EM structures revealed common features of the stalk domain forming three intra-oligomeric interfaces.

Just as in the apo structure, the monomer structure resolved after addition of nucleotides consists of a stalk domain that connects the BSE domain by the hinge 1 region followed by a hinge 2 connecting the BSE domain to the globular GD (Figure 2A). To compare the structures in more detail, we overlaid the structures with the previously solved apo structure and found that the GD is tilted upward by 4.3° and 4.6° in the presence of GDP or GTP, respectively (Figures 2B, 2C, and S1G). The GDs together with the BSE domain are rotated as a rigid body around hinge 1 as pivot point, while the rotation is restricted to a straight upward tilt without any sidewise rotation/tilt. When we compared the

Table 2. Cryo-EM data collection and processing

	*Syn*DLP WT	*Syn*DLP WT	*Sym*DLP MGD
	GTP	GDP	GMPPNP
Videos	4,560	6,149	5,087
Magnification	49kx	49kx	100kx
Voltage (kV)	200	200	200
Total dose (e^{-}/Å^2)	44.5	44.5	80.0
Defocus range (μm)	1.0–3.5	1.0–3.5	1.25–2.50
Super-resolution pixel size (Å)	0.8685	0.8685	0.408
Detector	Gatan K3 Bioquantum	Gatan K3 Bioquantum	Gatan K3 Bioquantum
Symmetry imposed	C2	C2	C2
Final no. of particles	279,572	395,948	219,630
Global map resolution (Å, FSC = 0.143)	3.6	4.1	3.8
Local map resolution range (Å, FSC = 0.5)	3.5–5.4	3.7 - 5.9	3.2–6.0
Initial model used (PDB code)	PDB: 7ZW6	PDB: 7ZW6	AF2 prediction
Model refinement			
Model resolution	3.7	4.3	3.7
CC mask	0.74	0.63	0.71
CC box	0.87	0.80	0.78
CC peaks	0.66	0.54	0.56
CC volume	0.72	0.61	0.70
CC ligands	–	–	0.85
Map-sharpening B-factor (Å^2)	−128.8	−165.8	−151.2
Model composition			
Nonhydrogen atoms	50,872	50,872	8,182
Protein residues	6,336	6,336	1,024
RMSDs			
Bond lengths (Å)	0.003	0.003	0.004
Bond angles (°)	0.842	0.848	0.754
Validation			
MolProbity score	1.24	1.38	1.46
Clash score	4.68	6.95	3.14
Rotamer outliers (%)	0.15	0.44	0.00
Ramachandran plot			
Favored (%)	98.35	98.20	94.88
Allowed (%)	1.65	1.80	5.12
Disallowed (%)	0.00	0.00	0.00
Deposition IDs			
EMDB	EMD-19812	EMD-19813	EMD-19814
PDB	PDB: 9EM7	PDB: 9EM8	PDB: 9EM9

structures with GDP or GTP, we also found a helix$_{131–147}$ kink in the periphery of the GD in addition to the rigid body rotation of the BSE and GD domain in the GDP structure (Figure 2D). This kink changes the orientation of helix$_{131–147}$ within the peripheral three-helix bundle. The observed changes in the GD orientations may have consequences for a potential head-to-head GD-GD contact, as observed for the GTP-bound state of classical dynamins.[17] Although we limited the incubation time to 5 min at room temperature (RT) instead of 30°C prior to plunge freezing, it is likely that *Syn*DLP consumed a large fraction of the supplied GTP. Limited by the low resolution in the G-domain, the corresponding cryo-EM density also does not support a bound nucleotide. Therefore, the observed domain shifts and rotations between the structures after addition of GTP may represent any transition state of nucleotide hydrolysis rather than a GTP-bound structure. In this context, hereafter we refer to the structure resolved from the GTP sample as *Syn*DLP in the presence of or after addition of GTP rather than a GTP (bound) structure.

Irregular SynDLP tubular structures form in the presence of lipid membranes

Previously, we have shown that *Syn*DLP binds to membranes containing negatively charged lipids.[38] To elucidate the *Syn*DLP-membrane interaction on a structural level, we analyzed

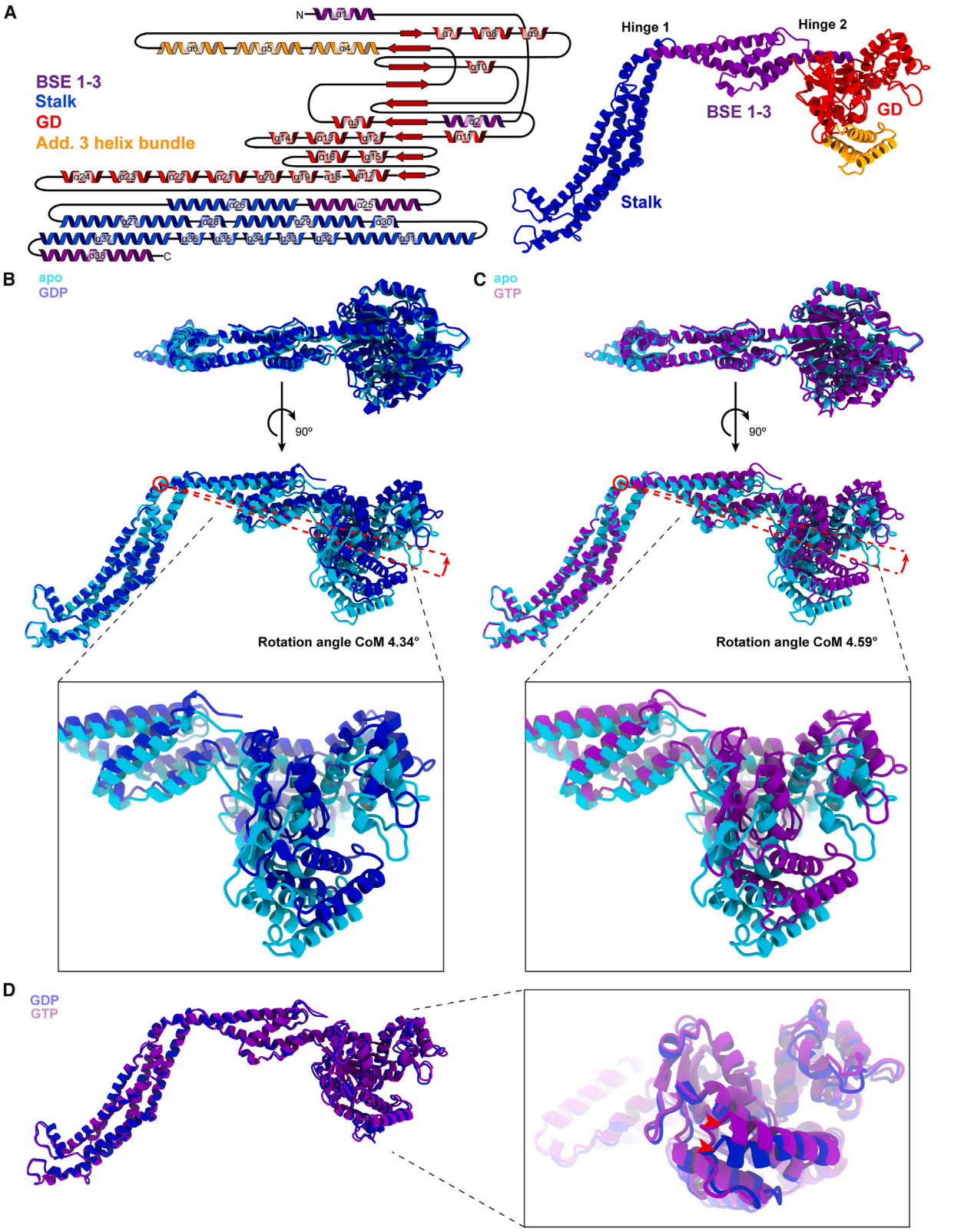

(legend on next page)

*Syn*DLP incubated with DOPG SUVs with or without nucleotides using cryo-EM. Upon incubation with SUVs, we observed flexible, crooked tubular structures with irregular features and diameters of 90–110 nm next to SUVs and occasionally proteinaceous density attached to otherwise ''naked'' SUVs without any apparent coat (Figure 3A). Upon incubation of *Syn*DLP/DOPG SUVs with GDP, we did not observe the irregular *Syn*DLP tubes anymore, instead we found single filamentous oligomers apparently not interacting with liposomes (Figure 3B). To mimic the GTP-bound state, we next incubated *Syn*DLP with DOPG SUVs plus GMPPNP (Figure 3C). Here, instead of the irregular *Syn*DLP tubes, we found smaller, less structured agglomerates of *Syn*DLP sitting close to lipid membranes. Given their heterogeneity, these assemblies can still be classified as elongated structures, and when found isolated, they have diameters of 40–50 nm. Their shape and appearance resemble the irregular *Syn*DLP tubes found in the apo state. In addition to the changes of the *Syn*DLP structure, we observed changes in the morphology of the membrane vesicles upon incubation with *Syn*DLP. In the micrographs of the apo and GMPPNP samples, we identified long extended vesicles of smooth texture and tubular shape presumably made of a continuous lipid membrane, while in the GDP sample, such shapes only occur rarely. We found 1–3 tubulated vesicles per 1.2-μm hole in both the apo and GMPPNP sample, with approximately 50–100 untubulated vesicles per hole. The length of the tubulated vesicles varied from approximately 200–800 nm in both samples. Interestingly, the tubule diameter in the apo sample was wider (approximately 40 nm) compared with the narrower tubes in the GMPPNP sample (approximately 25 nm).

As no protein density was identified on the membranes, the formation of these structures currently remains unclear. For a quantitative analysis of the changes in membrane morphology of individual vesicles, we statistically analyzed the vesicle circumferences of complete datasets of 200–800 micrographs per sample and included an additional control sample of DOPG-only SUVs (Figure S2C). In the control sample, the distribution of circumferences showed a peak at approximately 170 nm. We found that, upon addition of *Syn*DLP, an additional peak with a nearly doubled circumference emerged, resulting in, presumably, two major populations of 170 and 320 nm (Figure 3D), in line with the previous observation that *Syn*DLP induced vesicle fusion even in the absence of nucleotides.[38] A similar but stronger population shift was observed in the *Syn*DLP+GDP sample, while in the *Syn*DLP+GMPPNP sample, an almost complete shift to the 320-nm-circumference population was detected, indicating that nucleotides enhance the *Syn*DLP fusion activity. Due to the irregular nature of the tubular *Syn*DLP structures observed in the micrographs, a defined molecular assembly model cannot be determined experimentally. Nevertheless, as we only observed the irregular *Syn*DLP assemblies in the presence of lipid membranes, we conclude that the *Syn*DLP interaction with lipids triggers the formation of these tubular structures, possibly by associating with lipids.

Therefore, we re-examined our cryo-EM data of the apo sample to reconstruct larger oligomers at full length without using the segmentation approach. Typically, the filamentous oligomers had a variable length and, therefore, did not show a discrete oligomeric state. Although the resulting cryo-EM map had an overall poorer resolution (5–7 Å), we could rigidly place two copies of the determined atomic octamer models along the filament (Figure S2A). We determined the displacement shift and angle between the two octamer models and converted it to a helical rotation and rise of 8.178 Å and −6.156° for each dimeric asymmetrical unit (ASU) of the apo structure. When we applied the helical transformations to 20–40 ASUs, the resulting polymers formed a spring-like assembly with a diameter of approximately 106 nm (Figure S2B). After applying the same strategy to the structures determined in the presence of GDP and GTP, the resulting tubes had highly similar diameters of 97 nm and 94 nm, respectively. Importantly, the modeled tubes have dimensions similar to the irregular tubular assemblies observed after lipid interaction; i.e., diameters of 90–110 nm (Figure 3A). In support of this, similarly sized though non-regular tubes have been observed for other DLPs; i.e., Drp1.[31] Due to its interaction with negatively charged membranes, we hypothesized that *Syn*DLP interacts with negatively charged lipids via a positively charged stretch facing the lumen of the *Syn*DLP tubes (Figures S2D and S2E). Thus, to abrogate *Syn*DLP membrane binding, we mutated the RKxxR motif making up a positive binding stretch in the assembly. The mutated protein formed the intramolecular disulfide bond as well as oligomeric structures and was as GTPase active as the wild type (Figures S2F–S2H). While in our previous analyses, we had detected some changes in the membrane binding propensity, mutating the three positively charged residues to alanine had essentially no impact on membrane binding, demonstrating that the positively charged surface stretch on the concave surface of *Syn*DLP oligomers (i.e., in the inner lumen of [modeled] *Syn*DLP tubes) is not significantly involved in interaction with negatively charged membrane surfaces (Figure S2I).

The G-domain dimerizes by head-to-head GD-GD interactions

In the *Syn*DLP apo structure as well as in the structures with GDP or GTP, respectively, only small longitudinal GD interactions were observed. Typically, DLPs have additional transverse GD-GD contacts (i.e., inter-rung contacts via head-to-head GD-GD contacts)[19] that were not found in our experimental *Syn*DLP oligomer structures but are, in principle, possible based on our

Figure 2. Changes of the *Syn*DLP monomer structure upon nucleotide addition

(A) Domain architecture of *Syn*DLP: BSE1–BSE3 (violet), G-domain (GD) (red), three-helix bundle (orange), and stalk (blue).

(B and C) Comparison of the *Syn*DLP monomer structure in the apo (cyan) (PDB: 7ZW6) and GDP-bound (blue) state and upon addition of GTP (violet). In the presence of GDP, the GD is tilted upward by an angle of 4.34°. Upon addition of GTP, the GD is tilted upward by an angle of 4.59° (measured as center of mass rotation of the GD relative to the hinge between the stalk and BSE domain).

(D) Comparison of the *Syn*DLP monomer in the presence of GDP (blue) and GTP (violet). While the GD is mostly tilted as a rigid body in the presence of GDP, part of helix$_{131–147}$ shifts upward relative to the surrounding helix bundle upon addition of GTP (red arrowheads).

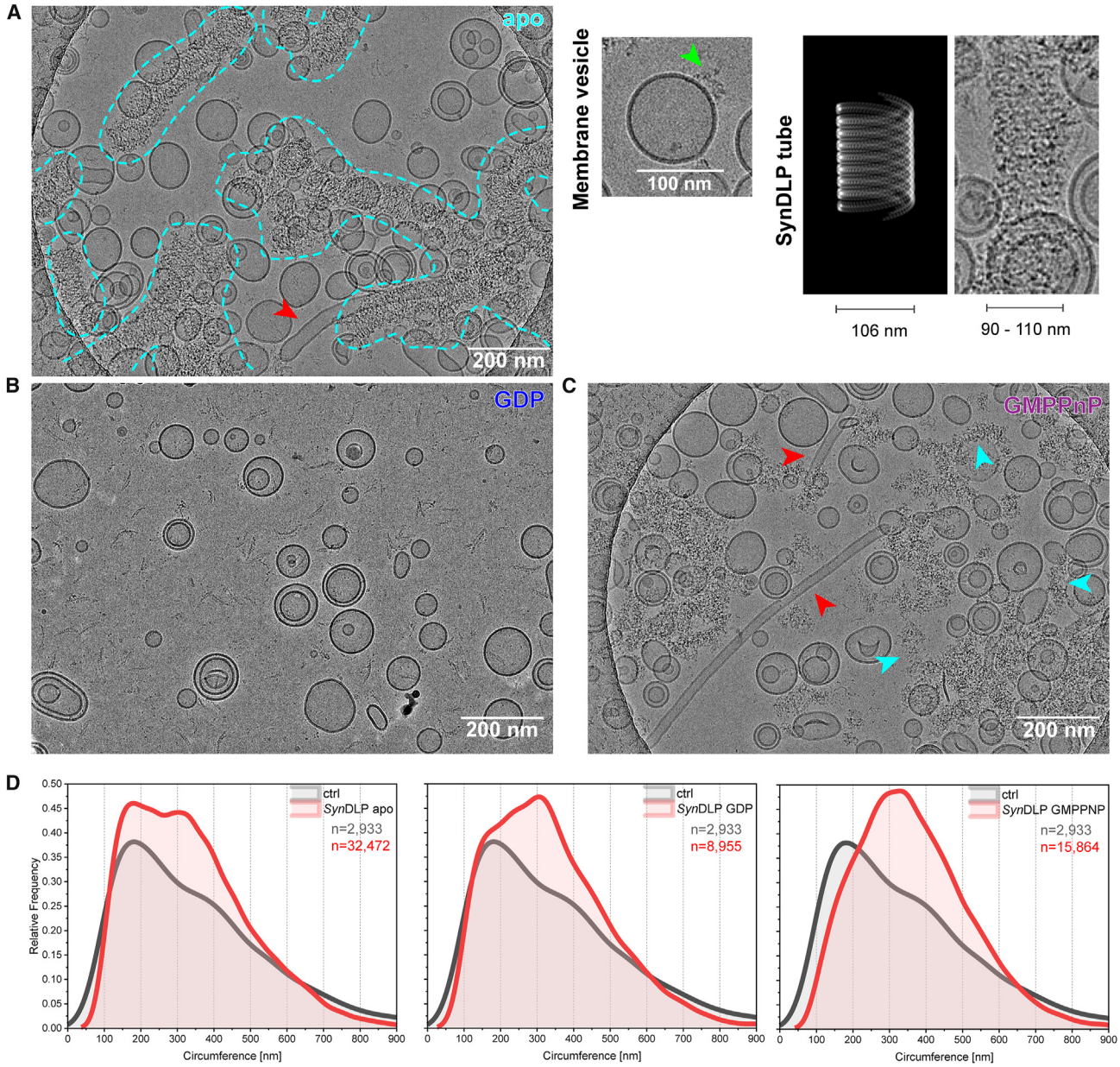

Figure 3. Interaction of *Syn*DLP with lipid membranes

(A) Left: cryo-EM micrograph of *Syn*DLP in the presence of DOPG SUVs. *Syn*DLP oligomers assemble to large crooked tubes with irregular features (indicated by cyan dashed lines). The red arrowhead indicates a tubulated vesicle. Right: magnified image of a membrane vesicle (a green arrowhead indicates proteinaceous density occasionally found close to vesicles) and *Syn*DLP tubes.

(B) Cryo-EM micrograph of *Syn*DLP in the presence of DOPG SUVs and GDP. *Syn*DLP oligomers remain in the filamentous oligomeric state.

(C) Cryo-EM micrograph of *Syn*DLP in the presence of DOPG SUVs and GMPPNP. *Syn*DLP oligomers assemble into elongated agglomerates (cyan arrowheads). Red arrowheads indicate extended tubulated vesicles.

(D) Analysis of the vesicle circumference observed in control vesicles in the absence of *Syn*DLP, vesicles in the presence of *Syn*DLP, *Syn*DLP+GDP, and *Syn*DLP+GMPPNP.

modeled structure of spring-like assembled oligomers and our enzymatic data (Figure S2). To test whether such transverse GD-GD interactions are putatively involved in the *Syn*DLP supramolecular organization and to enable the investigation of nucleotide-dependent changes in the GD on a structural level, we designed a truncated *Syn*DLP construct lacking the stalk domain responsible for longitudinal interactions in the oligomer. This minimal GD construct (*Syn*DLP MGD) consists solely of the GD and the BSE, with BSE2 and BSE3 connected by a short linker (Figure 4A). *Syn*DLP MGD formed an intact intramolecular

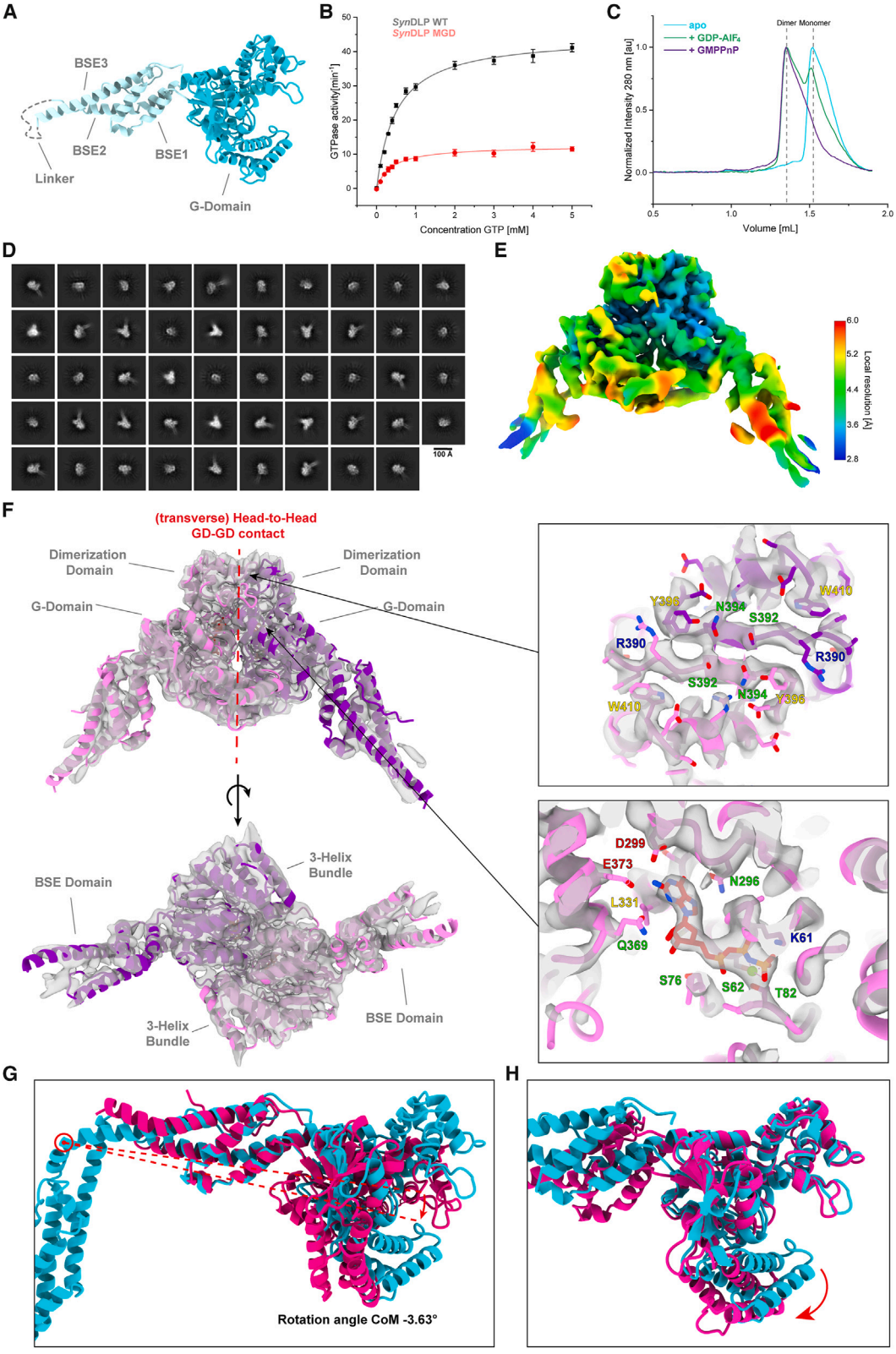

(legend on next page)

disulfide bridge in the BSE (Figure S3A), indicating proper folding of the protein. Strikingly, in the absence of longitudinal activating interactions, we determined a GTPase activity significantly lower than that of the full-length protein but still as high as ~10 min^{-1} (Figure 4B). Detected by size exclusion chromatography, the apo state of *Syn*DLP MGD formed monomers, whereas in the presence of the GTP analogs GMPPNP (mimicking the GTP-bound state) and GDP-AlF_4 (mimicking the transition state), *Syn*DLP MGD formed dimers (Figure 4C). Moreover, upon addition of GDP or GTP, *Syn*DLP MGD remained in the monomeric form, showing that GD-GD contacts do not form or persist after GTP hydrolysis (Figures S3B and S3C). These results suggest that the MGD construct dimerizes upon binding of a non-hydrolyzable GTP analog through transverse interactions to form GTPase-competent GDs.

To solve the structure of the *Syn*DLP MGD dimerized via GD-GD contacts, we plunge froze *Syn*DLP MGD after incubation with GMPPNP and subjected it to cryo-EM structure determination (Figure S3C). Based on the class averages showing distinct features and a two-fold symmetry (Figure 4D), we were able to solve the structure of the *Syn*DLP MGD dimer at a global resolution of 3.8 Å (Figure S3D). The local resolution in the periphery of the reconstruction was between 4.5 and 6.0 Å, while in the core of the reconstruction, the resolution was 3.6–4.0 Å (Figure 4E). The derived atomic model shows that the dimer interface is indeed formed via transverse (head-to-head) dimerization of the GD, and the BSE domains form arms projecting away from the dimer center (Figure 4F). The EM density in the center of the dimer, at the dimer interface, was of appropriate quality to model side chains and to place a model of the bound GMPPNP, revealing the surrounding catalytic residues. When we aligned the monomer of the full-length apo oligomer with the GMPPNP-bound MGD structure at the BSE domain, we found a downward tilt of the GD relative to the BSE domain by an angle of −3.6°, in contrast to the upward tilt of 4.3° and 4.6° of the GD in the oligomer structures with GDP and GTP, respectively (Figure 4G; see also Figure 2). When we aligned the structures at the GD, we found an additional displacement of the three-helix bundle relative to the GD (Figure 4H). This displacement moved the three-helix bundle toward the stalk/BSE domain, which, in turn, exposed the dimerization interface, enabling interaction of opposing monomers. The BSE domain does not appear to undergo major structural changes upon GMPPNP-induced dimerization in the MGD construct.

Upon inspection of the determined structure, we could identify the three-helix bundle (aa 105–174) at the periphery of the GD, in addition to an extended domain outside the catalytic core, which seemed to be involved in dimerization of the MGD construct (Figures 5A and 5B, left, blue dimerization domain, aa 330–422). When the catalytic core regions of the apo and GMPPNP-bound GDs were aligned, a shift of the switch I loop and a minor shift of the P loop in the catalytic core was observed, similar to what has been described for human Dynamin-1[17] (Figure S3E). When overlaying the full-length oligomer of the structure solved in the presence of GTP with the MGD dimer structure in a putative transversal head-to-head interaction of the GDs, unresolvable clashes occur. However, when the MGD conformations (without an opposing GD in head-to-head interaction) are overlaid with the oligomer structures, the observed molecular displacements can be accommodated within the half-moon-shaped oligomer (Figure S3F). Together, the observed MGD conformation is compatible with the full-length *Syn*DLP oligomer, whereas the transverse dimers observed with the MGD could not occur in the context of the determined *Syn*DLP oligomer structures due to steric clashes, suggesting a distinct reorganization of the monomers in a GTP-bound oligomer.

We compared the structure of the GD with that of human Dynamin-1 (PDB: 2X2E and 3ZYC)[17,42] (Figure 5A, right) and found that the BSE domain of *Syn*DLP MGD with bound GMPPNP is similar to the open conformation of the dynamin-1 BSE. We did not find any regions corresponding to the dimerization domain and the three-helix bundle in Dynamin-1, which is supported by sequence alignment of the respective GDs. The comparison reveals additional subdomains that correspond to the three-helix bundle and an extended dimerization domain (Figure S4). The catalytic cores of *Syn*DLP and Dynamin-1 are highly similar (root-mean-square deviation [RMSD] < 1 Å). Apart from the additional dimerization domain, the dimerization interface appears to be very similar between *Syn*DLP and Dynamin-1 (Figure 5B, right). In-depth comparison of the catalytic cores revealed that the switch I and P loop are similar, although the switch II and *trans*-stabilizing loop from the opposing monomer are shorter in *Syn*DLP than in Dynamin-1 (Figures 5C and 5D). Moreover, *Syn*DLP's residue D269 appears not to interact with the opposing switch I and P loop, whereas the corresponding residue D180 in Dynamin-1 is directly interacting with the opposing switch I and P loop. In addition, the G4 motif in *Syn*DLP is shorter than in Dynamin-1, and the G4 motifs of opposing monomers are further apart in *Syn*DLP, so there are no major *trans*-stabilizing interactions via the G4 motif. Although *Syn*DLP's *cis* interaction within the monomer of the guanine base

Figure 4. The MGD construct forms dimers in the presence of GTP analogs

(A) AlphaFold2-predicted structure of the minimal G-domain (MGD) construct, where the stalk domain has been removed (aa 474–748) and replaced by a linker of 9 aa.

(B) GTPase activity of *Syn*DLP WT (black) vs. *Syn*DLP MGD (red). Error bars represent SD; $n = 3$.

(C) Size-exclusion chromatogram of *Syn*DLP MGD in the absence (cyan) and presence of GDP-AlF_4 (green) or GMPPNP (violet). *Syn*DLP MGD in the absence of nucleotides forms monomers (1.54 mL). Discrete peaks for dimers (1.35 mL) and monomers (1.54 mL) were observed upon addition of GDP-AlF_4. In the presence of GMPPNP, *Syn*DLP MGD mainly forms dimers (1.35 mL).

(D) Class averages of *Syn*DLP MGD with bound GMPPNP.

(E) Local-resolution map of the cryo-EM structure of the *Syn*DLP MGD dimer with bound GMPPNP.

(F) Cryo-EM structure with the corresponding atomic ribbon model of the *Syn*DLP MGD dimer with bound GMPPNP. The top right inset shows details of the bound nucleotide GMPPNP, including relevant side chains, involving the previously identified catalytically relevant residue K61.[38] The bottom right inset shows details of the dimer interface.

(G and H) Comparison of the apo *Syn*DLP full length and the GMPPNP-bound MGD structure aligned at the BSE (G) and the GD (H).

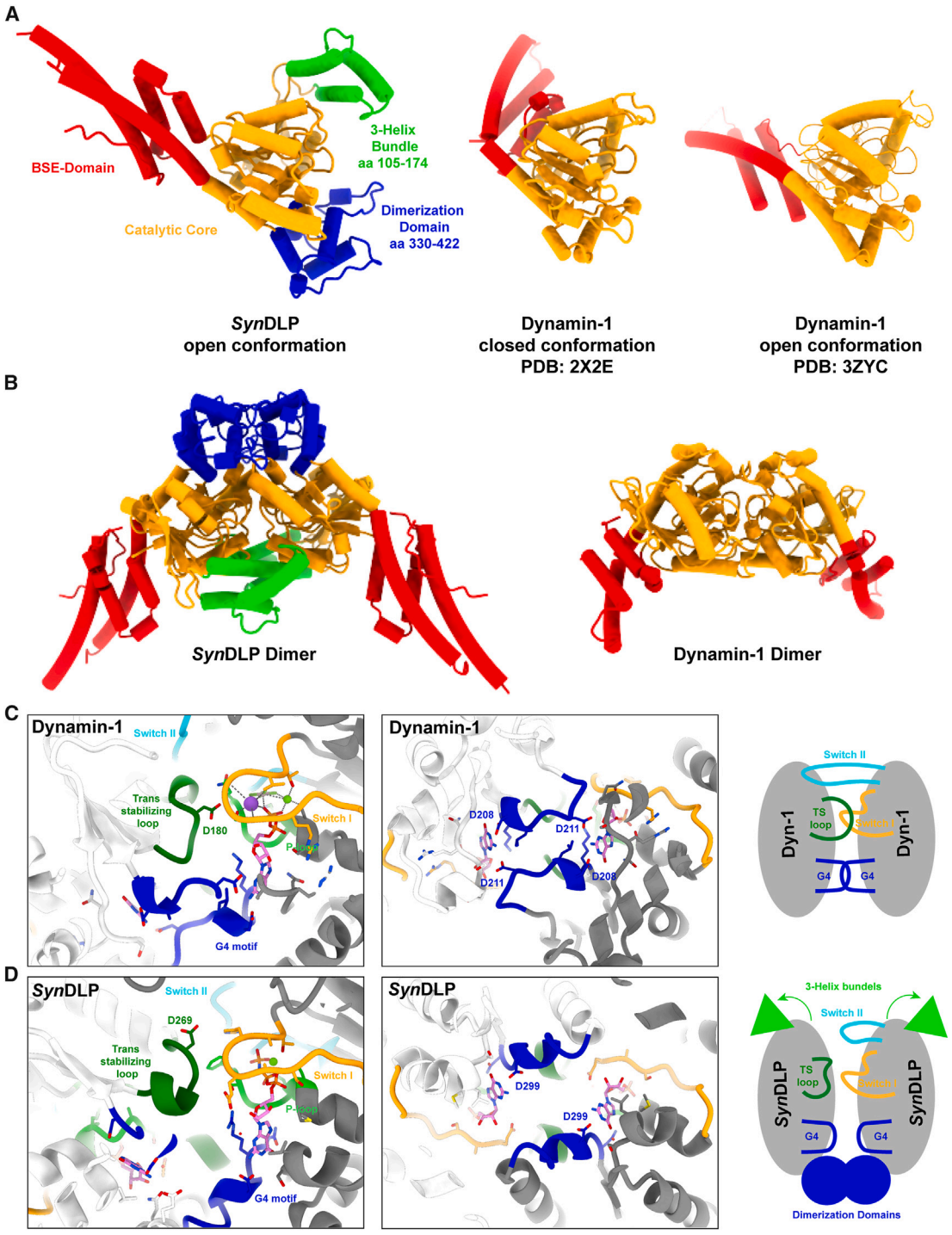

Figure 5. Comparison of the *Syn*DLP MGD dimer with the dynamin-1 dimer

(A) Domain architecture of the *Syn*DLP G-domain and comparison of the GDs of *Syn*DLP and Dynamin-1 in the closed and open conformation. The structures of the *Syn*DLP and Dynamin-1 catalytic cores (orange) are highly similar (RMSD 0.937 Å). The structure of the *Syn*DLP BSE (red) is similar to the Dynamin-1 BSE in the open conformation. The dimerization domain (blue) and three-helix-bundle (green) are not present in Dynamin-1.

(B) Models of GD dimers of *Syn*DLP (left) and Dynamin-1 (right). Models are colored by domain architecture.

(C and D) The dimer interface in the catalytic core of the GDs of Dynamin-1 (C) and *Syn*DLP (D). Left: comparison of switch I, the P loop, and the *trans*-stabilizing loop. Center: comparison of the G4 motifs. Right: simplified model of *trans*-stabilizing interactions in the respective head-to-head GD-GD dimers.

with D299 analogous to D208 in Dynamin-1 appears to be conserved, *trans* interaction could not be identified in the G4 motif of *Syn*DLP while being present for D211 in Dynamin-1. Instead, the *Syn*DLP GD dimer appears to be mainly stabilized by the extended additional dimerization domain. The catalytic core of *Syn*DLP contains less *trans*-stabilizing interactions compared to what has been observed thus far in DLPs, while the dimer is stabilized largely by an extra domain that is not present in classical dynamins.

DISCUSSION

In this study, we provide the structural basis for conformational adjustments mediated by GTP binding and/or hydrolysis by means of determined *Syn*DLP cryo-EM structures from short oligomers upon addition of GDP and GTP, respectively (Figure 1). We show that the presence of nucleotides led to tilting of the GD and BSE domain by ~4.5° in comparison with the previously resolved apo structure,[38] which, in turn, translates to a slightly altered oligomeric assembly architecture (Figure 2). Upon incubation of *Syn*DLP with DOPG vesicles, we experimentally observed formation of large tubular *Syn*DLP assemblies (Figure 3). Based on structural analyses of the oligomer, we developed an expanded *Syn*DLP model resulting in tubular assemblies with dimensions similar to the experimentally observed tubular structures. Moreover, we showed that *Syn*DLP GD-GD dimerization is mediated by an extended dimerization domain rather than via the *trans*-stabilizing loop and residues of the G4 motif, as observed for other DLPs (Figures 4 and 5).

Our analysis of the full-length *Syn*DLP structure with nucleotides was limited by the observation that GTP analogs cause formation of ill-defined *Syn*DLP assemblies as well as the high GTPase activity of *Syn*DLP. However, we observed small domain shifts and rotations between the full-length structures in the GDP and GTP-added samples. Therefore, the full-length structure solved after addition of GTP is likely a post-GTP hydrolysis structure. Oligomeric structures as observed for *Syn*DLP in its apo state or upon addition of GDP and GTP, respectively, have been observed for the mitochondrial DLP Drp1,[31] which forms tetramers and other small oligomers in the apo state. Nevertheless, upon addition of GTP, Drp1 (co-assembled with MID49) forms curved filamentous copolymers that can close to form ring-like structures, resembling the *Syn*DLP filamentous oligomers observed here. However, in the presence of the GTP analog GMPPCP, Drp1-MID49 copolymers extend to form linear filaments. The monomer structure of Drp1 in the linear filament is reminiscent of the *Syn*DLP full-length structures (with or without nucleotides) determined here.

In the filamentous *Syn*DLP oligomers, the GDs form stable longitudinal GD-BSE contacts that appear to be critical for the reported high GTPase activity.[38] In line with this observation, the MGD mutant lacking the ability to form longitudinal GD-BSE contacts showed significantly lowered GTPase activity. However, binding of a non-hydrolyzable GTP analog induces structural rearrangements, as observed with the MGD, leading to the formation of a *Syn*DLP head-to-head GD-GD dimer. GD dimerization of GTP-bound states, mimicked via binding of non-hydrolyzable GTP analogs such as GMPPNP, has also been shown for similar constructs of eukaryotic MGDs.[42,43] However, nucleotide-dependent dimerization of MGD constructs is typically observed in the presence of a transition state analog, such as GDP-AlF_4, as demonstrated for the eukaryotic DLPs Dynamin-1, MxA, Drp1, mitofusin 1, OPA1, Sey1p, atlastin, and Vps1.[17,33–36,43,44] As most eukaryotic DLPs form oligomeric filaments on membrane surfaces, resulting in the formation of membrane tubes, a low dimerization affinity in the GTP-bound state appears to be sufficient at the locally high monomer concentration to mediate GD-GD dimerization. A more stable GD-GD dimer is required during the power stroke.[45] In the case of *Syn*DLP, GTP binding (mimicked by GMPPNP) was found to trigger GD dimerization, whereas the MGD dimer was less stable with the transition state analog GDP-AlF_4. Of note, the yeast DLP Sey1p, which mediates fusion of the endoplasmic reticulum membrane, completely dimerizes in the presence of GMPPNP.[43] Together with the observations described here, these data indicate that an increased affinity of GD-GD dimerization in the GTP-bound state is critical for membrane remodeling triggered by fusogenic DLPs.

In comparison with human Dynamin-1, the *Syn*DLP catalytic core lacks critical *trans*-stabilizing features (shorter *trans*-stabilizing loop, switch II and G4 motif, fewer *trans*-stabilizing residues). Instead, *Syn*DLP GD dimerizes via its unique dimerization domain. Furthermore, the *Syn*DLP GD possesses an additional three-helix bundle,[38] and our analysis here shows that this three-helix bundle blocks head-to-head GD-GD dimerization in the *apo* state, while it appears to be displaced when GMPPNP is bound, enabling GD dimerization. Thus, the three-helix bundle is a regulatory domain that potentially controls GD-GD dimerization in a DLP subclass. Remarkably, analysis of cyanobacterial DLP sequences indicates that this three-helix-bundle appears to be conserved at least in the KGK (lysine-glycine-lysine domain) clade of cyanobacterial DLPs.[46] In contrast, we observed neither the three-helix bundle nor the extended dimerization domain in the published structures of other fusogenic DLPs, such as atlastin, Sey1p, Mgm1, mitofusin 1, and OPA1,[36,43,44,47,48] nor in other resolved prokaryotic DLPs structures from *Nostoc punctiforme* BDLP, IniA, *Campylobacter jejuni* DLP1/2, and LeoA.[11,12,28,49] Therefore, we currently cannot link the special structural characteristics of the *Syn*DLP GD identified here to other dynamin members or other protein functions, such as membrane fusion activity. Thus, to date, we consider these structural features to be unique.

In classical dynamin filaments (i.e., Dynamin-1[50]), head-to-head GD dimers connect two adjacent helical rungs through the *trans*-stabilizing loop that bridges from one GD to the nucleotide binding site of the opposing GD. Thereby, flexible switch regions within the catalytic core are stabilized, and the adjacent helical rungs are pulled together by a GTP-driven domain movement of the two hinges. The domain rearrangement allows sliding of adjacent rungs and dimerization with the next GD after binding a new GTP molecule and thus enables constriction of the dynamin filament. However, the structures of *Syn*DLP determined here reveal that this DLP is not capable of forming canonical head-to-head GD dimers in the apo state, as access to the GD is blocked by the longitudinal GD-GD contacts and the additional three-helix bundle. Nevertheless, the latter domain is displaced in the presence of the GTP analog GMPPNP, enabling

head-to-head GD-GD dimerization via the dimerization domain. However, the full-length oligomer structures of the apo state as well as in the presence of GDP and GTP are not compatible with formation of the head-to-head GD-GD interactions determined based on the MGD dimer because (1) the three-helix bundle of the opposing GD will clash with the stalk region of the oligomer and (2) the *Syn*DLP rung will cross with the opposing rung. Therefore, the *Syn*DLP oligomer possibly undergoes significant rearrangements involving the stalk domain to form a new oligomeric assembly upon GTP binding, or head-to-head interactions will either only be possible at the ends of oligomers or will lead to disassembly of the oligomers, at least in part. The latter is consistent with our observation that no filamentous oligomers were found in the GMPPCP and GMPPNP samples of the wild-type protein. Furthermore, the full-length *Syn*DLP likely also dimerizes via longitudinal GD-GD contacts. The full-length interaction cannot be described by a simple monomer-dimer model, as it appears to be more complex, in agreement with the observation that multiple and diverse oligomeric structures are involved in the *Syn*DLP activity. For Dynamin-1, it is thought that the constriction activity involves sliding of adjacent rungs and GD dimerization with the next GD after binding a new GTP molecule while retaining interactions in the stalk domain. Based on the data presented here, an analogous activity appears to be unlikely for *Syn*DLP.

Typically, DLPs use a combination of GTPase-driven conformational changes and mechanical force generated by their oligomerization to tubulate membranes and/or induce fission. The GTPase activity of DLPs leads to a conformational change that causes them to form helical assemblies around a membrane neck. Preceding the interaction with the membrane, prototypical dynamins, containing a relatively large Pleckstrin homology domain as MID, form an auto-inhibitory (tetrameric) oligomer that undergoes structural rearrangements to form a GTPase active assembly.[51,52] Formation of this assembly generates the mechanical force that increases the curvature of an enclosed membrane and eventually destabilizes a bilayer due to extreme curvature and subsequent constriction of the assembly. The induced curvature can either result in membrane fission (rupture of the tube at the destabilized bilayer) or membrane fusion (spontaneous connection of two opposing destabilized bilayers to release the curvature stress). In addition to transverse GD-GD contacts, the conformational changes during a GTP hydrolysis cycle include relative domain movements enabled by a pronounced flexibility of the two hinges. Noteworthy is that the exact conformational changes differ significantly among members of the dynamin superfamily.[20] DLP assemblies that tubulate membranes typically have outer diameters between 25 and 50 nm.[14] The diameter of the experimentally observed irregular tubes that form when *Syn*DLP is co-incubated with DOPG vesicles is 90–110 nm and, thus, significantly larger than most other comparable assemblies. Based on the analyzed micrographs, the identified *Syn*DLP tubes were not straight and did not form a regular array on continuous lipid tubules, as observed for other DLPs.[18,53,54] However, yeast Dnm1, which acts as a eukaryotic fission DLP at the outer mitochondrial membrane, forms protein tubes around appropriate membranes with an outer diameter of approximately 130 nm,[55] which is comparable to the size of *Syn*DLP tubes. Although we observed membrane tubules in the *Syn*DLP+DOPG sample that shrank from 40 to 25 nm upon addition of GMPPNP, we could not unambiguously observe *Syn*DLP-mediated constriction of tubes. Nevertheless, the *Syn*DLP monomers undergo substantial conformational rearrangements upon GTP binding, as suggested by our GMPPNP-bound MGD structure.

So far, we failed to identify a single membrane interaction site for *Syn*DLP, and the membrane-interacting residues of *Syn*DLP remain unidentified. It is well possible that multiple regions of the *Syn*DLP oligomers are involved in membrane binding. While other DLPs have defined MIDs that mediate membrane binding and subsequently trigger protein oligomerization, *Syn*DLP forms large homo-oligomers already in solution in the absence of membranes. For example, in Dynamin-1 or Drp1, oligomerization in solution is prevented by steric interference between the monomers caused by additional domains inserted into the stalk domain, such as the Pleckstrin homology domain (Dynamin-1) or an intrinsically disordered variable domain (Drp1).[56,57] However, *Syn*DLP shows a less complex domain arrangement without such additional domains, enabling protein oligomerization already in solution without the need for switching of domains induced by nucleotide and/or membrane binding. While we were unable to detect membrane-bound protein density of *Syn*DLP in our micrographs, occasionally proteinaceous density was found loosely attached to vesicles. However, as shown previously,[38] *Syn*DLP is binding to PG vesicles under the given conditions. Therefore, we reason that the membrane-bound form of *Syn*DLP is either too small and/or short lived to be visualized by cryo-EM. Another possibility is that the *Syn*DLP tubes observed here already represent the membrane-bound form of *Syn*DLP. Due to their irregular shape, it is possible that they have incorporated small membrane pieces or individual lipids in their tube lumen.

Like other DLPs, *Syn*DLP has been shown to destabilize PG-containing membranes, which enables liposome fusion *in vitro* in the absence of nucleotides.[38] By measuring the vesicle circumference under different conditions, we now show that *Syn*DLP is capable of membrane fusion in the absence of nucleotides (as shown before) as well as in the presence of GDP. The strongest increase in vesicle size and, therefore, membrane fusion was observed upon addition of GMPPNP. While *Syn*DLP clearly remodels membranes by fusing (and tubulating) vesicles in the absence of nucleotides, as also observed for *Bs*DynA, the fusogenic BDLP of *B. subtilis*, nucleotide binding and/or hydrolysis may well be involved in regulating the protein activity, as observed for *Bs*DynA.[10,40,58] Although *Syn*DLP destabilizes and remodels membranes, it is possibly involved in membrane repair processes caused by environmental stresses or phage infection, similar to *Bs*DynA acting against pore-forming antibiotics by fusing membranes.[10,58] Given the size of the *Syn*DLP tubes and its structural similarity to Drp1, it may also be possible that *Syn*DLP is involved in fusion/fission of large internal membrane systems; i.e., the cyanobacterial thylakoid membrane system during cell division.

In conclusion, our study provides insights into changes of the *Syn*DLP structure mediated by GTP binding and/or

hydrolysis. Initially, apo *Syn*DLP is organized in short, filamentous, half-moon-shaped oligomers in solution. In the presence of membranes, these *Syn*DLP oligomers form extended irregular tubes. GTP binding induces structural rearrangements in the GD and BSE domains, leading to GD dimerization, as shown here with a minimal GD construct. While the three-helix bundle partially blocks access to the nucleotide binding site in the apo state, it is displaced in the GMPPNP-bound state, enabling head-to-head dimerization via a unique dimerization domain. Further, we show that nucleotides may stimulate the membrane fusion activity of *Syn*DLP. Our study thus provides a basis for future research aiming to elucidate the mechanisms underlying BDLP-mediated membrane remodeling.

Limitations of this study

We monitored SynDLP-mediated membrane fusion of negatively charged liposomes in a previous study via DLS and a fluorescence resonance energy transfer (FRET)-based fusion assay[38] and in this study by cryo-EM imaging. Although SynDLP shifted the size of the vesicles to larger diameters, it is not clear how SynDLP mediates membrane fusion, as we could not clearly identify any prototypical fusion intermediates or membrane-attached protein density. Capturing these fusion intermediates is a challenging task, as the reaction appears to be either too fast or the intermediates are too short-lived/unstable to be captured by conventional plunge freezing and cryo-EM. One option to tackle this issue would be the creation of SynDLP mutations that slow down or halt the fusion process at specific stages (as has been done for eukaryotic DLPs before) or to use different nucleotide states to modify the fusion process in such a way that intermediates can be captured. Importantly, thus far we were unable to unambiguously identify a membrane binding domain in SynDLP. The analyses are complicated by SynDLP forming large oligomers already in solution, in the absence of membranes. Further analyses of SynDLP variants will help to eventually describe the mode by which SynDLP interacts with membranes. Further, we showed that the SynDLP MGD construct readily forms GD head-to-head dimers in the presence of nucleotide analogs, while the full-length protein only produces aggregates under the same conditions. The discrepancies between the MGD and full-length protein are somewhat enigmatic and suggest either rearrangement of the oligomers or disassembly of the oligomers upon GTP binding. Thus, this issue should be addressed in future experiments. Finally, while our previous and current analyses have enabled us to structurally describe SynDLP, its precise *in vivo* function remains to be elucidated.

STAR★METHODS

Detailed methods are provided in the online version of this paper and include the following:

SUPPLEMENTAL INFORMATION

Supplemental information can be found online at https://doi.org/10.1016/j.celrep.2024.114657.

ACKNOWLEDGMENTS

This study was funded by Deutsche Forschungsgemeinschaft (DFG) CRC1208 Project 267205415 (to C.S.) and CRC1552 Project 465145163 (to D.S.). The authors gratefully acknowledge the electron microscopy training, imaging, and access time granted by the life science EM facility of the Ernst-Ruska Center at Forschungszentrum Jülich. The authors gratefully acknowledge the computing time granted by the JARA Vergabegremium and provided on the JARA Partition part of the supercomputer JURECA at Forschungszentrum Jülich.[59] This work was funded by the Max-Planck Graduate Center at the Max Planck Institutes and the University of Mainz.

AUTHOR CONTRIBUTIONS

B.J., L.G., D.S., and C.S. designed research. L.G. and L.M. cloned, expressed, and purified the proteins. B.J. prepared cryo-EM samples, operated the electron microscopes, determined the cryo-EM structures, and built the refined atomic models. B.J. and P.S. analyzed the membrane morphology. L.G., L.M., R.J., and N.H. performed biochemical and biophysical analyses of the proteins. B.J., L.G., L.M., D.S., and C.S. prepared the manuscript.

DECLARATION OF INTERESTS

The authors declare no competing interests.

Received: July 8, 2023
Revised: April 23, 2024
Accepted: August 2, 2024

REFERENCES

1. Ban, T., Ishihara, T., Kohno, H., Saita, S., Ichimura, A., Maenaka, K., Oka, T., Mihara, K., and Ishihara, N. (2017). Molecular basis of selective mitochondrial fusion by heterotypic action between OPA1 and cardiolipin. Nat. Cell Biol. *19*, 856–863. https://doi.org/10.1038/ncb3560.
2. Findinier, J., Delevoye, C., and Cohen, M.M. (2019). The dynamin-like protein Fzl promotes thylakoid fusion and resistance to light stress in Chlamydomonas reinhardtii. PLoS Genet. *15*, e1008047. https://doi.org/10.1371/journal.pgen.1008047.
3. Gao, H., Sage, T.L., and Osteryoung, K.W. (2006). FZL, an FZO-like protein in plants, is a determinant of thylakoid and chloroplast morphology. Proc. Natl. Acad. Sci. USA *103*, 6759–6764. https://doi.org/10.1073/pnas.0507287103.
4. Hinshaw, J.E., and Schmid, S.L. (1995). Dynamin self-assembles into rings suggesting a mechanism for coated vesicle budding. Nature *374*, 190–192. https://doi.org/10.1038/374190a0.

5. Mettlen, M., Pucadyil, T., Ramachandran, R., and Schmid, S.L. (2009). Dissecting dynamin's role in clathrin-mediated endocytosis. Biochem. Soc. Trans. *37*, 1022–1026. https://doi.org/10.1042/BST0371022.

6. Orso, G., Pendin, D., Liu, S., Tosetto, J., Moss, T.J., Faust, J.E., Micaroni, M., Egorova, A., Martinuzzi, A., McNew, J.A., and Daga, A. (2009). Homotypic fusion of ER membranes requires the dynamin-like GTPase atlastin. Nature *460*, 978–983. https://doi.org/10.1038/nature08280.

7. Smirnova, E., Griparic, L., Shurland, D.L., and van der Bliek, A.M. (2001). Dynamin-related protein Drp1 is required for mitochondrial division in mammalian cells. Mol. Biol. Cell *12*, 2245–2256. https://doi.org/10.1091/mbc.12.8.2245.

8. Zhang, X., and Hu, J. (2009). Two small protein families, DYNAMIN-RELATED PROTEIN3 and FISSION1, are required for peroxisome fission in Arabidopsis. Plant J. *57*, 146–159. https://doi.org/10.1111/j.1365-313X.2008.03677.x.

9. van der Bliek, A.M. (1999). Functional diversity in the dynamin family. Trends Cell Biol. *9*, 96–102. https://doi.org/10.1016/s0962-8924(98)01490-1.

10. Bürmann, F., Ebert, N., van Baarle, S., and Bramkamp, M. (2011). A bacterial dynamin-like protein mediating nucleotide-independent membrane fusion. Mol. Microbiol. *79*, 1294–1304. https://doi.org/10.1111/j.1365-2958.2011.07523.x.

11. Liu, J., Noel, J.K., and Low, H.H. (2018). Structural basis for membrane tethering by a bacterial dynamin-like pair. Nat. Commun. *9*, 3345. https://doi.org/10.1038/s41467-018-05523-8.

12. Wang, M., Guo, X., Yang, X., Zhang, B., Ren, J., Liu, A., Ran, Y., Yan, B., Chen, F., Guddat, L.W., et al. (2019). Mycobacterial dynamin-like protein IniA mediates membrane fission. Nat. Commun. *10*, 3906. https://doi.org/10.1038/s41467-019-11860-z.

13. Praefcke, G.J.K., and McMahon, H.T. (2004). The dynamin superfamily: universal membrane tubulation and fission molecules? Nat. Rev. Mol. Cell Biol. *5*, 133–147. https://doi.org/10.1038/nrm1313.

14. Ford, M.G.J., and Chappie, J.S. (2019). The structural biology of the dynamin-related proteins: New insights into a diverse, multitalented family. Traffic *20*, 717–740. https://doi.org/10.1111/tra.12676.

15. Jimah, J.R., and Hinshaw, J.E. (2019). Structural Insights into the Mechanism of Dynamin Superfamily Proteins. Trends Cell Biol. *29*, 257–273. https://doi.org/10.1016/j.tcb.2018.11.003.

16. Gasper, R., Meyer, S., Gotthardt, K., Sirajuddin, M., and Wittinghofer, A. (2009). It takes two to tango: regulation of G proteins by dimerization. Nat. Rev. Mol. Cell Biol. *10*, 423–429. https://doi.org/10.1038/nrm2689.

17. Chappie, J.S., Acharya, S., Leonard, M., Schmid, S.L., and Dyda, F. (2010). G domain dimerization controls dynamin's assembly-stimulated GTPase activity. Nature *465*, 435–440. https://doi.org/10.1038/nature09032.

18. Low, H.H., Sachse, C., Amos, L.A., and Löwe, J. (2009). Structure of a Bacterial Dynamin-like Protein Lipid Tube Provides a Mechanism For Assembly and Membrane Curving. Cell *139*, 1342–1352. https://doi.org/10.1016/j.cell.2009.11.003.

19. Low, H.H., and Löwe, J. (2010). Dynamin architecture—from monomer to polymer. Curr. Opin. Struct. Biol. *20*, 791–798. https://doi.org/10.1016/j.sbi.2010.09.011.

20. Daumke, O., and Praefcke, G.J.K. (2016). Invited review: Mechanisms of GTP hydrolysis and conformational transitions in the dynamin superfamily. Biopolymers *105*, 580–593. https://doi.org/10.1002/bip.22855.

21. Kong, L., Sochacki, K.A., Wang, H., Fang, S., Canagarajah, B., Kehr, A.D., Rice, W.J., Strub, M.-P., Taraska, J.W., and Hinshaw, J.E. (2018). Cryo-EM of the dynamin polymer assembled on lipid membrane. Nature *560*, 258–262. https://doi.org/10.1038/s41586-018-0378-6.

22. Stowell, M.H., Marks, B., Wigge, P., and McMahon, H.T. (1999). Nucleotide-dependent conformational changes in dynamin: evidence for a mechanochemical molecular spring. Nat. Cell Biol. *1*, 27–32. https://doi.org/10.1038/8997.

23. Tuma, P.L., Stachniak, M.C., and Collins, C.A. (1993). Activation of dynamin GTPase by acidic phospholipids and endogenous rat brain vesicles. J. Biol. Chem. *268*, 17240–17246. https://doi.org/10.1016/S0021-9258(19)85328-0.

24. Warnock, D.E., Hinshaw, J.E., and Schmid, S.L. (1996). Dynamin Self-assembly Stimulates Its GTPase Activity. J. Biol. Chem. *271*, 22310–22314. https://doi.org/10.1074/jbc.271.37.22310.

25. Abutbul-Ionita, I., Rujiviphat, J., Nir, I., McQuibban, G.A., and Danino, D. (2012). Membrane Tethering and Nucleotide-dependent Conformational Changes Drive Mitochondrial Genome Maintenance (Mgm1) Protein-mediated Membrane Fusion. J. Biol. Chem. *287*, 36634–36638. https://doi.org/10.1074/jbc.C112.406769.

26. Accola, M.A., Huang, B., Al Masri, A., and McNiven, M.A. (2002). The Antiviral Dynamin Family Member, MxA, Tubulates Lipids and Localizes to the Smooth Endoplasmic Reticulum. J. Biol. Chem. *277*, 21829–21835. https://doi.org/10.1074/jbc.M201641200.

27. Bohuszewicz, O., and Low, H.H. (2018). Structure of a mitochondrial fission dynamin in the closed conformation. Nat. Struct. Mol. Biol. *25*, 722–731. https://doi.org/10.1038/s41594-018-0097-6.

28. Low, H.H., and Löwe, J. (2006). A bacterial dynamin-like protein. Nature *444*, 766–769. https://doi.org/10.1038/nature05312.

29. Muriel, M.-P., Dauphin, A., Namekawa, M., Gervais, A., Brice, A., and Ruberg, M. (2009). Atlastin-1, the dynamin-like GTPase responsible for spastic paraplegia SPG3A, remodels lipid membranes and may form tubules and vesicles in the endoplasmic reticulum. J. Neurochem. *110*, 1607–1616. https://doi.org/10.1111/j.1471-4159.2009.06258.x.

30. Gao, S., von der Malsburg, A., Paeschke, S., Behlke, J., Haller, O., Kochs, G., and Daumke, O. (2010). Structural basis of oligomerization in the stalk region of dynamin-like MxA. Nature *465*, 502–506. https://doi.org/10.1038/nature08972.

31. Kalia, R., Wang, R.Y.-R., Yusuf, A., Thomas, P.V., Agard, D.A., Shaw, J.M., and Frost, A. (2018). Structural basis of mitochondrial receptor binding and constriction by DRP1. Nature *558*, 401–405. https://doi.org/10.1038/s41586-018-0211-2.

32. Reubold, T.F., Faelber, K., Plattner, N., Posor, Y., Ketel, K., Curth, U., Schlegel, J., Anand, R., Manstein, D.J., Noé, F., et al. (2015). Crystal structure of the dynamin tetramer. Nature *525*, 404–408. https://doi.org/10.1038/nature14880.

33. Rennie, M.L., McKelvie, S.A., Bulloch, E.M.M., and Kingston, R.L. (2014). Transient Dimerization of Human MxA Promotes GTP Hydrolysis, Resulting in a Mechanical Power Stroke. Structure *22*, 1433–1445. https://doi.org/10.1016/j.str.2014.08.015.

34. Varlakhanova, N.V., Alvarez, F.J.D., Brady, T.M., Tornabene, B.A., Hosford, C.J., Chappie, J.S., Zhang, P., and Ford, M.G.J. (2018). Structures of the fungal dynamin-related protein Vps1 reveal a unique, open helical architecture. J. Cell Biol. *217*, 3608–3624. https://doi.org/10.1083/jcb.201712021.

35. Wenger, J., Klinglmayr, E., Fröhlich, C., Eibl, C., Gimeno, A., Hessenberger, M., Puehringer, S., Daumke, O., and Goettig, P. (2013). Functional mapping of human dynamin-1-like GTPase domain based on x-ray structure analyses. PLoS One *8*, e71835. https://doi.org/10.1371/journal.pone.0071835.

36. Yu, C., Zhao, J., Yan, L., Qi, Y., Guo, X., Lou, Z., Hu, J., and Rao, Z. (2020). Structural insights into G domain dimerization and pathogenic mutation of OPA1. J. Cell Biol. *219*, e201907098. https://doi.org/10.1083/jcb.201907098.

37. Anand, R., Eschenburg, S., and Reubold, T.F. (2016). Crystal structure of the GTPase domain and the bundle signalling element of dynamin in the GDP state. Biochem. Biophys. Res. Commun. *469*, 76–80. https://doi.org/10.1016/j.bbrc.2015.11.074.

38. Gewehr, L., Junglas, B., Jilly, R., Franz, J., Zhu, W.E., Weidner, T., Bonn, M., Sachse, C., and Schneider, D. (2023). SynDLP is a dynamin-like

protein of Synechocystis sp. PCC 6803 with eukaryotic features. Nat. Commun. *14*, 2156. https://doi.org/10.1038/s41467-023-37746-9.

39. Bramkamp, M. (2018). Bacterial dynamin-like proteins reveal mechanism for membrane fusion. Nat. Commun. *9*, 3993. https://doi.org/10.1038/s41467-018-06559-6.
40. Guo, L., Sattler, L., Shafqat, S., Graumann, P.L., and Bramkamp, M. (2021). A Bacterial Dynamin-Like Protein Confers a Novel Phage Resistance Strategy on the Population Level in Bacillus subtilis. mBio *13*, e0375321. https://doi.org/10.1128/mbio.03753-21.
41. Guo, L., and Bramkamp, M. (2019). Bacterial dynamin-like protein DynA mediates lipid and content mixing. Faseb. J. *33*, 11746–11757. https://doi.org/10.1096/fj.201900844RR.
42. Chappie, J.S., Mears, J.A., Fang, S., Leonard, M., Schmid, S.L., Milligan, R.A., Hinshaw, J.E., and Dyda, F. (2011). A Pseudoatomic Model of the Dynamin Polymer Identifies a Hydrolysis-Dependent Powerstroke. Cell *147*, 209–222. https://doi.org/10.1016/j.cell.2011.09.003.
43. Yan, L., Sun, S., Wang, W., Shi, J., Hu, X., Wang, S., Su, D., Rao, Z., Hu, J., and Lou, Z. (2015). Structures of the yeast dynamin-like GTPase Sey1p provide insight into homotypic ER fusion. J. Cell Biol. *210*, 961–972. https://doi.org/10.1083/jcb.201502078.
44. Yan, L., Qi, Y., Huang, X., Yu, C., Lan, L., Guo, X., Rao, Z., Hu, J., and Lou, Z. (2018). Structural basis for GTP hydrolysis and conformational change of MFN1 in mediating membrane fusion. Nat. Struct. Mol. Biol. *25*, 233–243. https://doi.org/10.1038/s41594-018-0034-8.
45. Ganichkin, O.M., Vancraenenbroeck, R., Rosenblum, G., Hofmann, H., Mikhailov, A.S., Daumke, O., and Noel, J.K. (2021). Quantification and demonstration of the collective constriction-by-ratchet mechanism in the dynamin molecular motor. Proc. Natl. Acad. Sci. USA *118*, e2101144118. https://doi.org/10.1073/pnas.2101144118.
46. Jilly, R., Khan, N.Z., Aronsson, H., and Schneider, D. (2018). Dynamin-Like Proteins Are Potentially Involved in Membrane Dynamics within Chloroplasts and Cyanobacteria. Front. Plant Sci. *9*, 206. https://doi.org/10.3389/fpls.2018.00206.
47. Byrnes, L.J., and Sondermann, H. (2011). Structural basis for the nucleotide-dependent dimerization of the large G protein atlastin-1/SPG3A. Proc. Natl. Acad. Sci. USA *108*, 2216–2221. https://doi.org/10.1073/pnas.1012792108.
48. Faelber, K., Dietrich, L., Noel, J.K., Wollweber, F., Pfitzner, A.-K., Mühleip, A., Sánchez, R., Kudryashev, M., Chiaruttini, N., Lilie, H., et al. (2019). Structure and assembly of the mitochondrial membrane remodelling GTPase Mgm1. Nature *571*, 429–433. https://doi.org/10.1038/s41586-019-1372-3.
49. Michie, K.A., Boysen, A., Low, H.H., Møller-Jensen, J., and Löwe, J. (2014). LeoA, B and C from Enterotoxigenic Escherichia coli (ETEC) Are Bacterial Dynamins. PLoS One *9*, e107211. https://doi.org/10.1371/journal.pone.0107211.
50. Liu, J., Alvarez, F.J.D., Clare, D.K., Noel, J.K., and Zhang, P. (2021). CryoEM structure of the super-constricted two-start dynamin 1 filament. Nat. Commun. *12*, 5393. https://doi.org/10.1038/s41467-021-25741-x.
51. Antonny, B., Burd, C., De Camilli, P., Chen, E., Daumke, O., Faelber, K., Ford, M., Frolov, V.A., Frost, A., Hinshaw, J.E., et al. (2016). Membrane fission by dynamin: what we know and what we need to know. EMBO J. *35*, 2270–2284. https://doi.org/10.15252/embj.201694613.
52. Song, B.D., Leonard, M., and Schmid, S.L. (2004). Dynamin GTPase Domain Mutants That Differentially Affect GTP Binding. J. Biol. Chem. *279*, 40431–40436. https://doi.org/10.1074/jbc.M407007200.
53. Melo, A.A., Sprink, T., Noel, J.K., Vázquez-Sarandeses, E., van Hoorn, C., Mohd, S., Loerke, J., Spahn, C.M.T., and Daumke, O. (2022). Cryo-electron tomography reveals structural insights into the membrane remodeling mode of dynamin-like EHD filaments. Nat. Commun. *13*, 7641. https://doi.org/10.1038/s41467-022-35164-x.
54. Takeda, T., Kozai, T., Yang, H., Ishikuro, D., Seyama, K., Kumagai, Y., Abe, T., Yamada, H., Uchihashi, T., Ando, T., and Takei, K. (2018). Dynamic clustering of dynamin-amphiphysin helices regulates membrane constriction and fission coupled with GTP hydrolysis. Elife *7*, e30246. https://doi.org/10.7554/eLife.30246.
55. Mears, J.A., Lackner, L.L., Fang, S., Ingerman, E., Nunnari, J., and Hinshaw, J.E. (2011). Conformational changes in Dnm1 support a contractile mechanism for mitochondrial fission. Nat. Struct. Mol. Biol. *18*, 20–26. https://doi.org/10.1038/nsmb.1949.
56. Lu, B., Kennedy, B., Clinton, R.W., Wang, E.J., McHugh, D., Stepanyants, N., Macdonald, P.J., Mears, J.A., Qi, X., and Ramachandran, R. (2018). Steric interference from intrinsically disordered regions controls dynamin-related protein 1 self-assembly during mitochondrial fission. Sci. Rep. *8*, 10879. https://doi.org/10.1038/s41598-018-29001-9.
57. Srinivasan, S., Dharmarajan, V., Reed, D.K., Griffin, P.R., and Schmid, S.L. (2016). Identification and function of conformational dynamics in the multidomain GTPase dynamin. EMBO J. *35*, 443–457. https://doi.org/10.15252/embj.201593477.
58. Sawant, P., Eissenberger, K., Karier, L., Mascher, T., and Bramkamp, M. (2016). A dynamin-like protein involved in bacterial cell membrane surveillance under environmental stress. Environ. Microbiol. *18*, 2705–2720. https://doi.org/10.1111/1462-2920.13110.
59. Thörnig, P. (2021). JURECA: Data Centric and Booster Modules implementing the Modular Supercomputing Architecture at Jülich Supercomputing Centre. Journal of large-scale research facilities JLSRF *7*, A182. https://doi.org/10.17815/jlsrf-7-182.
60. Rueden, C.T., Schindelin, J., Hiner, M.C., DeZonia, B.E., Walter, A.E., Arena, E.T., and Eliceiri, K.W. (2017). ImageJ2: ImageJ for the next generation of scientific image data. BMC Bioinf. *18*, 529. https://doi.org/10.1186/s12859-017-1934-z.
61. Punjani, A., Rubinstein, J.L., Fleet, D.J., and Brubaker, M.A. (2017). cryoSPARC: algorithms for rapid unsupervised cryo-EM structure determination. Nat. Methods *14*, 290–296. https://doi.org/10.1038/nmeth.4169.
62. Emsley, P., Lohkamp, B., Scott, W.G., and Cowtan, K. (2010). Features and development of Coot. Acta Crystallogr. D Biol. Crystallogr. *66*, 486–501. https://doi.org/10.1107/S0907444910007493.
63. Afonine, P.V., Poon, B.K., Read, R.J., Sobolev, O.V., Terwilliger, T.C., Urzhumtsev, A., and Adams, P.D. (2018). Real-space refinement in PHENIX for cryo-EM and crystallography. Acta Cryst D *74*, 531–544. https://doi.org/10.1107/S2059798318006551.
64. Afonine, P.V., Klaholz, B.P., Moriarty, N.W., Poon, B.K., Sobolev, O.V., Terwilliger, T.C., Adams, P.D., and Urzhumtsev, A. (2018). New tools for the analysis and validation of cryo-EM maps and atomic models. Acta Cryst D *74*, 814–840. https://doi.org/10.1107/S2059798318009324.
65. Tegunov, D., and Cramer, P. (2019). Real-time cryo-electron microscopy data preprocessing with Warp. Nat. Methods *16*, 1146–1152. https://doi.org/10.1038/s41592-019-0580-y.
66. Goddard, T.D., Huang, C.C., Meng, E.C., Pettersen, E.F., Couch, G.S., Morris, J.H., and Ferrin, T.E. (2018). UCSF ChimeraX: Meeting modern challenges in visualization and analysis. Protein Sci. *27*, 14–25. https://doi.org/10.1002/pro.3235.
67. Croll, T.I. (2018). ISOLDE: a physically realistic environment for model building into low-resolution electron-density maps. Acta Cryst D *74*, 519–530. https://doi.org/10.1107/S2059798318002425.
68. Jakobi, A.J., Wilmanns, M., and Sachse, C. (2017). Model-based local density sharpening of cryo-EM maps. Elife *6*, e27131. https://doi.org/10.7554/eLife.27131.
69. Jumper, J., Evans, R., Pritzel, A., Green, T., Figurnov, M., Ronneberger, O., Tunyasuvunakool, K., Bates, R., Žídek, A., Potapenko, A., et al. (2021). Highly accurate protein structure prediction with AlphaFold. Nature *596*, 583–589. https://doi.org/10.1038/s41586-021-03819-2.
70. Gibson, D.G., Young, L., Chuang, R.-Y., Venter, J.C., Hutchison, C.A., and Smith, H.O. (2009). Enzymatic assembly of DNA molecules up to several hundred kilobases. Nat. Methods *6*, 343–345. https://doi.org/10.1038/nmeth.1318.

71. Heidrich, J., Wulf, V., Hennig, R., Saur, M., Markl, J., Sönnichsen, C., and Schneider, D. (2016). Organization into higher ordered ring structures counteracts membrane binding of IM30, a protein associated with inner membranes in chloroplasts and cyanobacteria. J. Biol. Chem. *291*, 14954–14962. https://doi.org/10.1074/jbc.M116.722686.

72. Monod, J., Wyman, J., and Changeux, J.-P. (1965). On the nature of allosteric transitions: A plausible model. J. Mol. Biol. *12*, 88–118. https://doi.org/10.1016/S0022-2836(65)80285-6.

73. Terwilliger, T.C., Sobolev, O.V., Afonine, P.V., and Adams, P.D. (2018). Automated map sharpening by maximization of detail and connectivity. Acta Cryst D *74*, 545–559. https://doi.org/10.1107/S2059798318004655.

74. Pettersen, E.F., Goddard, T.D., Huang, C.C., Meng, E.C., Couch, G.S., Croll, T.I., Morris, J.H., and Ferrin, T.E. (2021). UCSF ChimeraX: Structure visualization for researchers, educators, and developers. Protein Sci. *30*, 70–82. https://doi.org/10.1002/pro.3943.

75. Williams, C.J., Headd, J.J., Moriarty, N.W., Prisant, M.G., Videau, L.L., Deis, L.N., Verma, V., Keedy, D.A., Hintze, B.J., Chen, V.B., et al. (2018). MolProbity: More and better reference data for improved all-atom structure validation. Protein Sci. *27*, 293–315. https://doi.org/10.1002/pro.3330.

76. Morin, A., Eisenbraun, B., Key, J., Sanschagrin, P.C., Timony, M.A., Ottaviano, M., and Sliz, P. (2013). Collaboration gets the most out of software. Elife *2*, e01456. https://doi.org/10.7554/eLife.01456.

77. Ronneberger, O., Fischer, P., and Brox, T. (2015). U-Net: Convolutional Networks for Biomedical Image Segmentation. Preprint at arXiv. https://doi.org/10.48550/arXiv.1505.04597.

78. Zhang, T.Y., and Suen, C.Y. (1984). A fast parallel algorithm for thinning digital patterns. Commun. ACM *27*, 236–239. https://doi.org/10.1145/357994.358023.

STAR★METHODS

KEY RESOURCES TABLE

REAGENT or RESOURCE	SOURCE	IDENTIFIER
Bacterial and Virus Strains		
E. coli Rosetta-gami (DE3)	Novagen	71136–3
Chemicals, Peptides, and Recombinant Proteins		
*Syn*DLP	This study	UniprotKB: P73765
*Syn*DLP MGD	This study	NA
*Syn*DLP-RKxxR-A	This study	NA
DOPG	AvantiPolarLipids	Cat#840475C
DOPC	AvantiPolarLipids	Cat#850375C
Laurdan	Sigma-Aldrich	Cat#40227
GTP	Sigma-Aldrich	Cat#51120-1G
GDP	Sigma-Aldrich	Cat#G7127-1G
GMPPNP	Jena-Bioscience	Cat#NU-401-50
GMPPCP	Jena-Bioscience	Cat#NU-402-25
Deposited Data		
*Syn*DLP+GDP structure	This study	PDB: 9EM7 EMD-19812
*Syn*DLP+GTP structure	This study	PDB: 9EM8 EMD-19813
*Syn*DLP MGD+GMPPNP structure	This study	PDB: 9EM9 EMD-19814
*Syn*DLP apo structure	Gewehr et al[38]	PDB: 7ZW6 EMD-14993
Dynamin-1 MGD	Chappie et al.[17]	PDB: 2X2E
Dynamin-1 MGD	Chappie et al.[42]	PDB: 3ZYC
Oligonucleotides		
Primers	see Table S1	NA
Recombinant DNA		
pET303-*slr0869*-CT/His	Gewehr et al.[38]	NA
pET303-*slr0869*-CT/His SynDLP MGD	This study	NA
pET303-*slr0869*-CT/His *Syn*DLP-RKxxR-A	This study	NA
Software and Algorithms		
ImageJ	Rueden et al.[60]	https://imagej.nih.gov/ij/
OriginPro2023b	OriginLabCorp.	https://www.originlab.com/
cryoSPARC v3	Punjani et al.[61]	https://cryosparc.com/
Coot0.9	Emsley et al.[62]	https://www2.mrc-lmb.cam.ac.uk/personal/pemsley/coot/
Phenix	Afonine et al.[63,64]	https://phenix-online.org/
WARP	Tegunov and Cramer[65]	http://www.warpem.com/warp/
EPU	ThermoFisher Scientific	https://www.thermofisher.com/de/de/home/electron-microscopy/products/softwareem-3d-vis/epu-software.html
UCSF ChimeraX	Goddard et al.[66]	https://rbvi.ucsf.edu/chimerax/
ISOLDE	Croll[67]	https://tristanic.github.io/isolde/

(*Continued on next page*)

Continued

REAGENT or RESOURCE	SOURCE	IDENTIFIER
LocSCALE	Jakobi et al.[68]	https://gitlab.tudelft.nl/aj-lab/locscale
AlphaFold2	Jumper et al.[69]	https://github.com/google-deepmind/alphafold
Other		
Quantifoil Grids R1.2/1.3 Cu 200 mesh	Electron Microscopy Sciences	Cat#Q210CR1.3
Quantifoil Grids R2/1 Au 200 mesh	Electron Microscopy Sciences	Cat#Q210AR1
Quantifoil Grids R2/1 Cu 200 mesh	Electron Microscopy Sciences	Cat#Q210CR1

RESOURCE AVAILABILITY

Lead contact

Further information and requests for resources and reagents should be directed to and will be fulfilled by the lead contact, Carsten Sachse (c.sachse@fz-juelich.de).

Materials availability

All unique and stable reagents generated in this study are available from the lead contact with a completed Material Transfer Agreement.

Data and code availability

- The EMDB accession numbers for cryo-EM maps and *Syn*DLP models are EMD-19812, EMD-19813, EMD-19814 and PDB: 9EM7, 9EM8, 9EM9.
- This paper does not report original code.
- Any additional information required to reanalyze the data reported in this paper is available from the lead contact upon request.

EXPERIMENTAL MODEL AND STUDY PARTICIPANT DETAILS

E. coli Rosetta-gami (DE3) transformed with the respective plasmids (see key resource table) were grown at 37°C in LB medium until an OD600 of 0.6–0.8 was reached with appropriate antibiotic supplementation. Expression of *Syn*DLP was induced via addition of IPTG (1 mM). Cells were grown at 20°C overnight, harvested by centrifugation.

METHOD DETAILS

Expression and purification of SynDLP

*Syn*DLP WT (ORF *slr0869* of *Synechocystis* sp. PCC 6803) and *Syn*DLP-RKxxR-A were expressed in *E. coli* Rosetta-gami (DE3) using pET303-CT/His plasmids. The cell pellet was resuspended in buffer (50 mM NaH_2PO_4, 300 mM NaCl, 10% glycerol, 10 mM imidazole, pH 8.0). After homogenization with a Potter-Elvehjem device cells were lysed with an LM20 microfluidizer (Microfluidics international cooperation, Westwood, MA, USA) for four rounds at a pressure of 18,000 psi. The crude cell extract was centrifuged (15,000g, 10 min, 4°C) and the supernatant was mixed with a Ni-NTA matrix (Protino, Macherey-Nagel, Düren, Germany). After incubation at 4°C for 2 h, the matrix was washed six times with the same buffer supplemented with either 20 mM, 40 mM or 50 mM imidazole, respectively. *Syn*DLP was finally eluted with buffer containing 500 mM imidazole. After addition of 0.2 mM DTT, the proteins were further purified via gel filtration using a Sephacryl S-400 HR column (Cytiva, Freiburg, Germany) equilibrated with 20 mM HEPES pH 7.4, 0.2 mM DTT on an ÄKTA purifier 10 system (GE Healthcare, Munich, Germany). Protein concentrations were determined using a reducing agent compatible BCA assay kit (PierceTM, Thermo Fisher Scientific, Darmstadt, Germany). For expression of the *Syn*DLP minimal G-domain construct (*Syn*DLP-MGD), the pET303-*slr0869*-CT/His plasmid was mutated via Gibson assembly[70] (primers in Table S1). *Syn*DLP-MGD was expressed and purified analogous to *Syn*DLP except that the gel filtration step was performed using a Superdex 200 Hi-Load 16/600 column (Cytiva, Freiburg, Germany) with some exceptions: The cell pellet was incubated with 25 μg/mL lysozyme for 30 min prior to cell lysis. The purification included only four washing steps with buffer supplemented with 20 mM or 40 mM imidazole, respectively.

Liposome preparation and lipid reconstitution

Dioleoyl-*sn*-glycero-3-phospho-(1′-rac-glycerol) (DOPG) and 1,2-dioleoyl-*sn*-glycero-3-phosphocholine (DOPC) dissolved in chloroform were purchased from Avanti polar lipids (Alabaster, Alabama, USA). Lipid films were produced by evaporating the solvent under a gentle stream of nitrogen and vacuum desiccation overnight. The lipid films were rehydrated in 5 mM $MgCl_2$, 7.5 mM KCl, 20 mM HEPES pH 7.4 by shaking for 30 min at 37°C. The resulting liposome solution was subjected to five freeze-thaw cycles, combined

with sonication at 37°C in a bath sonicator. SUVs (small unilamellar vesicles) were generated by extrusion of the liposome solution through a porous polycarbonate filter (100 nm pores). For *Syn*DLP lipid reconstitution, *Syn*DLP was added to DOPG SUVs together with or without 1 mM nucleotides and incubated at RT for 3 h. Then the mixture was applied to TEM grids and plunge frozen (see below). In the membrane binding experiments, DOPC/DOPG (70:30) liposomes were used. Laurdan (Sigma-Aldrich, Munich, GER) was added at a molar ratio of 1:500 to the lipid mixture in the organic solvent ($CHCl_3$/MeOH 2:1 (v/v)). The lipid film was completely dried by evaporating the solvent under a nitrogen stream and vacuum desiccation overnight. Liposomes were prepared by hydrating the lipid film in storage buffer (20 mM HEPES, 0.2 mM DTT, pH 7.4) and via freezing in liquid nitrogen and thawing at 37°C, repeated five times.

Membrane binding assay

The fluorescent dye Laurdan (6-dodecanoyl-N,N-dimethyl-2-naphthylamine) is a lipophilic probe that incorporates into lipid bilayers. It can be used to analyze interactions of proteins with membranes via monitoring changes in the membrane lipid order upon addition of protein.[38,71] Polarity changes in the fluorophores environment caused by protein adhesion to the membrane surface result in changes of the Laurdan emission spectra. 0.1 mM DOPC/DOPG (70:30) liposomes were incubated with 0.5 μM protein and without protein in buffer for 1h at RT. Laurdan fluorescence emission spectra were recorded from 400 to 550 nm at 25°C with excitation at 350 nm using a Fluoromax-4 spectrometer (Horiba Scientific, Kyoto, JPN). The excitation and emission slit widths were adapted to a spectral resolution of 3 nm. The data were analyzed with MS Excel (Office 365) and OriginTM (OriginLab Corporation, Northampton, MA, USA). After subtraction of a buffer blank spectrum, the generalized polarization value (GP) value was calculated via Equation 1:

$$GP = (I_{440} - I_{490}) / (I_{440} + I_{490}) \quad \text{(Equation 1)}$$

I_{440} and I_{490} represent the Laurdan fluorescence emission intensities at 440 and 490 nm. To obtain the ΔGP values, the value determined with liposomes in absence of protein was subtracted.

GTPase assay

GTPase activity was measured using a modified version of a continuous, regenerative and coupled GTPase assay. Reaction buffer (final concentrations: 20 mM HEPES pH 7.4, 150 mM NaCl, 7.5 mM KCl, 5 mM $MgCl_2$, 0.2 mM DTT) was mixed with phosphoenolpyruvate (final concentration: 1 mM). 2.33% v/v PK/LDH (Sigma-Aldrich Chemie GmbH, Taufkirchen, Germany) and NADH (final concentration: 0.6 mM) (Carl Roth GmbH & Co. KG, Karlsruhe, Germany) were added to obtain a master mix. Different concentrations of GTP (Sigma-Aldrich Chemie GmbH, Taufkirchen, Germany) dissolved in 20 mM HEPES pH 7.4 were added to the master mix, and the solutions were incubated at 4°C for 15 min to convert all remaining GDP to GTP. The protein (0.5 μM final concentration) and pure buffer (blank) were placed into a 96-well plate and mixed with the GTP-containing master mix, resulting in a final volume of 150 μL per well. The absorption at 340 nm was observed over 2–3 h with a microplate reader (FLUOstar Omega, BMG Labtech GmbH, Ortenberg, Germany) at 30°C. The activities at different substrate concentrations were calculated as follows: The absolute value of the slope of the blank measurement was subtracted from the absolute value of the maximum linear absorption decrease at 340 nm, yielding the corrected decrease of the absorption at 340 nm over time (Δacorr). The GTP hydrolyzing activity was calculated with Equation 2:

$$Activity = \frac{\Delta A_{corr}}{d * \varepsilon * c_{protein}} \quad \text{(Equation 2)}$$

ε refers to the molar extinction coefficient of NADH at 340 nm (6220 M^{-1} cm^{-1}) and d is the thickness of 150 μL sample volume in a 96-well plate (0.38 cm). The calculated activities were plotted against the GTP concentrations. The data points were fitted with a Michaelis-Menten equation (Equation 3) to determine the turnover rate (kcat) and the Michaelis-Menten constant (Km).

$$Activity([GTP]) = \frac{[GTP] * k_{cat}}{[GTP] + K_m} \quad \text{(Equation 3)}$$

When the inhibitor guanosine-5′-[β,γ-imido]triphosphate (GMPPNP) was used, *Syn*DLP (final concentration: 0.25 μM) was incubated for 15 min at RT in the presence of the 0 mM, 0.05 mM, 0.1 mM or 0.3 mM GMPPNP before the remaining assay components were added. The steady-state kinetics of the *Syn*DLP GTPase activity revealed a cooperative behavior in the presence of GMPPNP (as further outlined in the text). Consequently, the experimental data were analyzed based on the Monod-Wyman-Changeux (MWC) model.[72] In the MWC model, it is assumed that cooperativity arises from the concerted transition of *n* functionally coupled subunits (the allosteric unit) from a low affinity T-state to a high affinity R-state upon increase of substrate concentration. Cooperativity is observed only, if in the absence of substrate (or ligand) the T-state strongly dominates. If the R-state prevails, no or only weak cooperativity is observed. In the MWC model, an inhibitor preferentially binds to the T-state, shifting the conformational distribution to the T-state, thus more substrate is needed to populate the R-state. The steady-state kinetic observed at different GMPPNP concentrations were analyzed by globally fitting Equation 4 to the data:

$$Activity([GTP]) = \frac{[GTP] * \left(a_R * (1 + K_R * [GTP] + Z_R * [GMPPnP])^{n-1} + a_T * L(1 + K_T * [GTP] + Z_T * [GMPPnP])^{n-1}\right)}{(1 + K_R * [GTP] + Z_R * [GMPPnP])^n + L * (1 + K_T * [GTP] + Z_T * [GMPPnP])^n} \quad \text{(Equation 4)}$$

Here, L is the allosteric equilibrium constant that describes the ratio of the concentration of allosteric units in the T- and R-state in the absence of substrate or inhibitor: $L = [T_0]/[R_0]$. The affinity of substrate and inhibitor for the R and T-states are K_R (K_T) and Z_R (Z_T), respectively. Additionally, the catalytic activity might differ for the R and the T-state, denoted by V_R and V_T, respectively. For numerical reasons, the products V_RK_R and V_TK_T are treated as individual parameter in the fit, denoted by a_R and a_T, respectively. N is the number of allosteric subunits and was set to a fixed value before the fit. In this way, varying values of n were tested and the resulting fit curves were evaluated with regard to how they match the experimental data points based on the value of r^2.

Sedimentation assay

0.5 μM *Syn*DLP was incubated for 30 min at 4°C in reaction buffer. Optionally, 2 mM nucleotide (GTP, GDP, GMPPNP) was added before the incubation. Reactions were centrifuged in a TLA-100 rotor (Beckman Coulter GmbH, Krefeld, Germany) at 4°C, 60,000g for 30 min using an Optima MAX-XP ultracentrifuge (Beckman Coulter GmbH, Krefeld, Germany). Supernatant (S) and pellet (P) were analyzed by sodium dodecyl sulfate polyacrylamide gel electrophoresis (SDS-PAGE) followed by Coomassie staining. *Syn*DLP band intensities were determined using the software Fiji-ImageJ.[60] Relative intensities were calculated by dividing supernatant or pellet band intensity by the sum of supernatant and pellet band intensity.

Size exclusion chromatography

*Syn*DLP-MGD (10 μM) was incubated in reaction buffer with 2 mM nucleotides at 4°C. The transition state analog GDP-AlF_4 was generated from a mixture of 2 mM GDP, 2 mM $AlCl_3$ and 20 mM NaF. After 30 min incubation, a Superdex 200 3.2/300 column (Cytiva, Uppsala, Sweden), equilibrated with reaction buffer, was loaded with 30 μL of the reactions. Proteins were eluted using an ÄKTA purifier 10 system (GE Healthcare, Munich, Germany) at 7°C and a flow rate of 0.04 mL/min). Typical standard proteins (Figure S3B) were used for protein size estimation.

ANS fluorescence thermal shift assay

For the fluorescence thermal shift assay, *Syn*DLP (5 μM) was mixed with 50 μM of the fluorophore 8-anilinonaphthalene-1-sulfonic acid (ANS) in reaction buffer in the absence or presence of 2 mM nucleotide. Fluorescence emission was recorded from 400 to 600 nm using a JASCO FP-8500 fluorescence spectrometer (JASCO cooperation, Tokyo, Japan) upon excitation at 370 nm. Integration time was 0.1 s and the excitation and emission slits were set to 2.5 nm. Spectra were recorded with a scan rate of 200 nm/min, 1 nm steps at temperatures ranging from 20°C to 80°C in 1°C steps and a heating rate of 1°C/min. The fluorescence intensity at 470 nm was used as a measure of the *Syn*DLP folding state. Three independent measurements were combined for each sample. The datasets were interpolated due to different actual temperatures and then averaged to obtain a melting curve of the protein. The transition temperature was determined using an adapted Boltzmann fit (Equation 5):

$$F_{meas}(T) = \frac{(T * m_N + F_N) - (T * m_D + F_D)}{1 + e^{\frac{T - T_m}{dT}}} + (T * m_D + F_D) \quad \text{(Equation 5)}$$

F_{meas} denotes the measured fluorescence intensity at 470 nm, while T is the temperature. F_N and F_D are the fluorescence intensities at the plateau regions of the native and the denatured protein, m_N and m_D are the slopes of the corresponding plateaus. It is important to note that fitting using Equation 5 could not be applied to the entire measured temperature range, as the ANS fluorescence strongly depends on the temperature besides binding to a folded or denatured protein. Therefore, the adjusted data includes a temperature range of 20°C–25°C capturing the transition phase.

Electron cryomicroscopy

*Syn*DLP was incubated with 1 mM GTP or GDP in in 5 mM $MgCl_2$, 7.5 mM KCl, 20 mM HEPES pH 7.4 for 5 min at RT and stored on ice for plunge freezing (20 min max). Grids were prepared by applying 3.5 μL *Syn*DLP to glow-discharged (PELCO easiGlow Glow Discharger, Ted Pella Inc.) Quantifoil grids (R1.2/1.3 or R2/1 Cu or Au 200 mesh, Electron Microscopy Sciences). The grids were plunge-frozen in liquid ethane using a ThermoFisher Scientific Vitrobot Mark IV set to 90% humidity at 10°C (blotting force −5, blotting time 3 to 3.5 s, 30 s preincubation on the grid for sample containing DOPG). Movies were recorded on a 200 kV Talos Arctica G2 (ThermoFisher Scientific) electron microscope equipped with a Bioquantum K3 (Gatan) detector operated by EPU (ThermoFisher Scientific).

The *Syn*DLP MGD sample was incubated with 2 mM GMPPNP for 45 min at 4°C. Then the sample was applied to SEC to isolate the dimer fraction (Superdex 200 10/300 column, elution buffer: 150 mM NaCl, 0.2 mM DTT, 5 mM MgCl2, 7.5 mM KCl, 20 mM HEPES pH 7.4). Fractions of the dimer peak were pooled, concentrated to 3.5 mg/mL and immediately plunge frozen. 4.0 μL sample were applied to glow-discharged (PELCO easiGlow Glow Discharger, Ted Pella Inc.) Quantifoil grids (R1.2/1.3 Cu 200 mesh, Electron Microscopy Sciences). The grids were plunge-frozen in liquid ethane using a Leica EM GP2 set to 70% humidity at 10°C (sensor guided backside-blotting, blotting time 4 s). Movies were recorded on a 200 kV Talos Arctica G2 (Thermofisher Scientific) electron microscope equipped with a Bioquantum K3 (Gatan) detector operated by EPU (ThermoFisher Scientific).

Sample and data collection details are included in Table 1.

Cryo-EM image processing

*Syn*DLP WT: Movie frames in super resolution were gain corrected, dose weighted and aligned using cryoSPARC Live.[61] All following image processing steps were performed using cryoSPARC. The steps were similar for the GTP and GDP dataset. Particles were picked using the template picker with the 20 Å low-pass filtered *Syn*DLP *apo* map (EMD-14993)[38] as template. The picked particles were extracted with a box size of 450 px and Fourier cropped to 256 px. The extracted particles stack was cleaned up by multiple rounds of 2D classification. An *ab-initio* reconstruction was created from these particles and further refined by multiple rounds of non-uniform refinements and heterogeneous refinements. The particles from the last step were then re-extracted at full resolution (450 px box size with 0.8685 Å voxel spacing), subjected to a last round of heterogeneous refinement and non-uniform refinement with defocus and CTF refinement to correct for higher order aberrations. The resolution of the final reconstructions was determined by Fourier shell correlation (auto-masked, FSC = 0.143) (Figure S1C). The local resolution distribution and local filtering was performed using cryoSPARC.

*Syn*DLP MGD: Movie frames were binned to the physical pixel size, gain corrected, dose weighted and aligned using WARP.[65] All following image processing steps were performed using cryoSPARC.[61] Initially, particles of a 350-micrograph subset were picked using a blob picker (146 Å blobs). The nine best-looking 2D classes of these particles were used as templates for a template-based picker. The picked particles were extracted with a box size of 300 px (245 Å) and Fourier cropped to 100 px. The extracted particles stack was cleaned up by multiple rounds of 2D classification. The final particle subset contained only classes that could be successfully centered on a single particle. These particles were extracted with a 450 px box (367 Å). A two-class *ab-initio* job was performed to further clean the particle stack in 3D, followed by multiple rounds of heterogeneous refinement. The particles from the last step were subjected to non-uniform refinement with imposed C2 symmetry and then subjected to defocus and CTF refinement to correct for higher order aberrations. To relax the imposed symmetry, a symmetry expansion job followed by local refinement without imposed symmetry was used. The resolution of the final reconstructions was determined by Fourier shell correlation (auto-masked, FSC = 0.143) (Figure S3D). The local resolution distribution and local filtering was performed using cryoSPARC.

Cryo-EM map interpretation and model building

The 3D reconstructions were B-factor sharpened in phenix (*phenix.auto-sharpen*).[73] The handedness of the final map was determined by rigid-body fitting the structure of *Syn*DLP (PDB:7ZW6)[38] into the final maps using ChimeraX[66,74] and flipped accordingly. PDB: 7ZW6 was MDFF fitted to the 3D reconstructions using ISOLDE.[67] Then an assembly of eight monomer copies was built to fit the whole map. The assembly models were subjected to auto-refinement with *phenix.real_space_refine*[63](with NCS constraints and NCS refinement). After auto-refinement the models were used for local model based map sharpening with LocSCALE[68] to produce the final maps. The auto-refined models were checked/adjusted manually in Coot[62] before a final cycle of auto-refinement with *phenix.real_space_refine*[63](with NCS constraints and NCS refinement). After final inspection, the model was validated in *phenix.validation_cryoem*[64]*/Molprobity*[75]. The same procedure was used for building of the *Syn*DLP MGD dimer model, except that a AlphaFold2[69] prediction of the dimer was used as initial model.

To create the structures of fully assembled *Syn*DLP tubes, two octameric assembly were fitted to the density of uncropped *Syn*DLP half-moon shaped oligomers (see Figure S2A) and measuring the displacement and rotation axis between the central dimers of each octamer. This refers to a displacement of four asymmetric units, therefore the measured rotation and rise were divided by four to get the helical symmetry parameters for the asymmetric units. These parameters were then applied to the dimer (the asymmetric unit) to create the structural model of the fully assembled *Syn*DLP tubes. Image processing and model building was completed using SBGrid-supported applications.[76] Cryo-EM structure determination and model refinement details are given in Table 2.

Analysis of membrane images

For characterization of the membrane morphology, SUV only (control), SUVs with *Syn*DLP, *Syn*DLP+GDP, and *Syn*DLP+GMPPNP datasets were analyzed. Statistical analysis of the membrane features was performed on segmentations of the micrographs. Multiple micrographs from each dataset were manually segmented at a pixel size of 7 Å and given as patches as a training dataset to a standard U-Net[77] with a depth of 4, patch size of 256, kernel size of 3 and batch size of 32. The micrographs were divided into patches, normalized to a mean of 0 and a standard deviation of 1, and simple rotations (90°, 180°, 270°) as well as flipped patches were added as data augmentation. The individual membranes are represented as the skeleton of their segmentation,[78] and highly aggregated or overlapping sections of the images were discarded as the automatic identification of the membrane shapes was ambiguous. Furthermore, only closed-segmented vesicles were analyzed. The circumference of a vesicle was estimated by calculating the sum of the distances between neighboring points of the skeleton.

QUANTIFICATION AND STATISTICAL ANALYSIS

Data and statistical analysis were performed using OriginPro 2023b (OriginLab Corp., Northampton, USA). Detailed descriptions of quantifications and statistical analyses (exact values of *n*, dispersion and precision measures used and statistical tests used) can be found in the respective Figures, Figure legends and Methods section.